Sedimentologika

10.57035/journals/sdk.2026.e41.1914

Origin and composition of the Siderolithic Group, Geneva Basin (GEo-02 well)

Aurélia Crinière [1], **Yasin Makhloufi** [1], **Ovie Emmanuel Eruteya** [1], **and Andrea Moscariello*** [1]

[1]Geo-Energy Group, Department of Earth Sciences, University of Geneva, Rue des Maraîchers 13, 1205, Geneva, Switzerland

CRediT statement: *Writing-original draft*: AC. *Writing-review & editing*: AC, OEE, AM, YM. *Visualization*: AC. *Conceptualization*: AC, AM. *Data curation*: AC. *Formal analysis*: AC. *Investigation*: AC. *Resources*: AC. *Validation*: AM, YM. *Supervision*: AM, YM. *Funding acquisition*: AM.

*Corresponding author: Andrea Moscariello, andrea.moscariello@unige.ch

Abstract

This study provides new insights into the Siderolithic Group, a 158 m-thick sedimentary succession deposited within a regionally extensive karstified unconformity spanning tens of square kilometres. This unconformity marks the Cretaceous-Paleogene boundary, with a stratigraphic gap of about 94 Myr, ranging from the Lower Cretaceous (Barremian–Aptian) to (likely) the Bartonian (Eocene). Using borehole data from the GEo-02 geothermal exploration well in the Geneva Basin, our study integrates petrography, mineralogy, geochemistry, and petrophysical analyses of 139 samples to reconstruct the evolution of this complex depositional system. Six sedimentological subunits were identified, representing distinct phases of karst evolution, from initial formation to infill and subsequent diagenesis. Variations in gamma ray values suggest fluctuating water levels within the karst system, while the heterogeneous distribution of quartz grains indicates detrital sediment input from both aeolian and fluvial sources. The mineral assemblage, dominated by siderite, chlorite, and kaolinite, reflects diagenetic processes under reducing conditions, with siderite facilitating kaolinite chloritisation in the presence of quartz. Geochemical data and clay mineral data indicate humid climatic conditions during deposition. The Siderolithic Group is inferred to be of Bartonian age based on biostratigraphic constraints from analogue deposits on the Swiss Plateau, suggesting its deposition during the Middle Eocene Climatic Optimum (MECO). This study provides one of the few continental records of the MECO in Western Europe, recording high mercury content possibly related to the flare-up in Neotethys subduction zone volcanism.

Research Article

Executive Editor
Giovanna Della Porta

Associate Editor
Daniel Petrash

Reviewers
Two anonymous reviewers

Production Manager
Jarred Lloyd

Copy Editor
Seyedeh Mortazavi

Received: 2025-03-23
Accepted: 2025-10-17
Published: 2026-01-20

Keywords
Karst
K-Pg
Middle Eocene Climatic Optimum (MECO)
Geneva Basin
Siderolithic

Plain language summary

As part of the GEothermies program, the GEo-02 geothermal exploration well was drilled in 2018–2019 in the Geneva Basin, Switzerland. This study identifies unique, 158-metre-thick continental deposits known as the Siderolithic Group, and provides valuable insight into the geological history of the region and is being explored for heat storage. Using multi-analytical methods, this study reveals how tectonic activity and climate changes shaped its formation, leading to karst development, erosion, and a hiatus of about 94 Myr, followed by continental infill during the Eocene. These findings suggest the Siderolithic Group could be one of the few known Bartonian-age continental records linked to the Middle Eocene Climatic Optimum (MECO), a poorly understood period of global warming.

Résumé

Cette étude apporte de nouvelles données sur le Groupe Sidérolithique, une succession sédimentaire de 158 m d'épaisseur déposée sur une grande discordance régionale. Cette discontinuité marque l'intervalle stratigraphique Crétacé-Paléogène, avec un hiatus d'environ 94 Myr, entre le Crétacé inférieur (Barrémien–Aptien) et (probablement) le Bartonien (Eocène). À partir des données du forage GEo-02 dans le Bassin genevois, nous avons combiné des analyses pétrographiques, minéralogiques, géochimiques et pétrophysiques sur 139 échantillons pour reconstituer l'évolution de ce système de dépôt complexe. Six sous-unités sédimentologiques ont été identifiées, indiquant une séquence d'événements de dépôt en tant que remplissage karstique, ce qui a permis de reconstruire l'évolution du karst à partir de sa formation, de son remplissage et des processus diagénétiques ultérieurs. Les unités sidérolithiques présentent des valeurs variables de rayons gamma, ce qui suggère des fluctuations du niveau d'eau dans le karst pendant le dépôt. La distribution hétérogène des grains de quartz reflète une histoire complexe impliquant des dépôts éoliens et fluviatiles, indiquant un remplissage du karst influencé par divers processus sédimentaires. L'association de sidérite, de chlorite et de kaolinite implique des processus diagénétiques nécessitant des ions ferreux et carbonates, ainsi que la chloritisation de la kaolinite en présence de sidérite et de quartz. Les données géochimiques et la minéralogie des argiles indiquent des conditions climatiques humides au moment de la formation du Sidérolithique. Son âge probable du Bartonien, basé sur la contrainte biostratigraphique des dépôts analogues du Plateau suisse, suggère un dépôt pendant l'optimum climatique de l'Éocène moyen (MECO). Cette étude fournit l'un des rares enregistrements continentaux du MECO en Europe occidentale, avec une teneur élevée en mercure, qui pourrait être liée à une intensification de l'activité volcanique associée à la zone de subduction de la Néotéthys.

1 Introduction

Understanding the subsurface of sedimentary basins in terms of lithology, mineralogical composition, diagenetic history, and petrophysical properties is fundamental, particularly for geothermal energy applications. In Switzerland, the Geneva Basin (Figure 1A) has been characterised as a low-enthalpy region, with an average geothermal gradient of 25 to 30 °C km^{-1} and a heat flow ranging from 64 to 82 mW m^{-2} (Chelle-Michou et al., 2017). Geothermal development stalled after the unsuccessful drilling of the Thônex well in 1993 (Jenny et al., 1995) but has regained interest as Geneva advances its strategy for sustainable heat production, especially for industrial processes and district heating (Moscariello et al., 2020).

The Siderolithic Group in the Geneva Basin presents a promising geothermal reservoir, as it overlies a widespread karstified zone associated with a significant unconformity at the top of the Lower Cretaceous carbonate formations (Charollais et al., 2007, 2023; Moscariello, 2019). The karst system may enhance permeability through interconnected cavities, while the quartz-rich sandstone and terra rossa-type paleosols infill could provide sufficient porosity for fluid storage and heat exchange, making the system potentially suitable for geothermal applications. Similar paleokarst systems have been recognised as promising geothermal reservoirs in various geological settings, such as the Carboniferous in the UK (Narayan et al., 2021; Pharaoh et al., 2021) and the Malm aquifer beneath the Molasse Basin in the Alpine Foreland (Bohnsack et al., 2020; Hörbrand et al.,

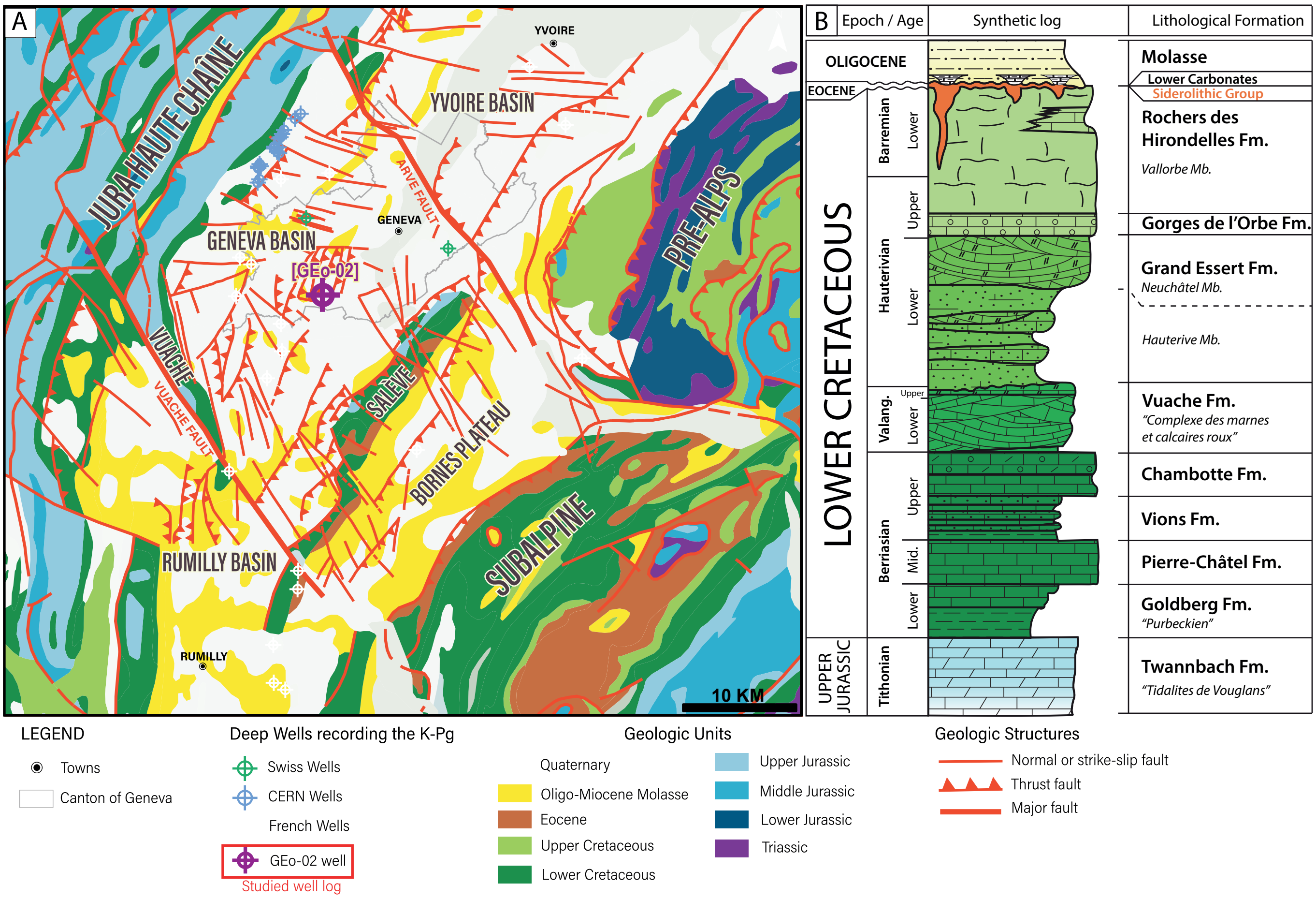

Figure 1 – Location of the study area in the trans-border Swiss-French Geneva Basin. **(A)** Structural map showing the distribution of major faults (Clerc & Moscariello, 2020) and deep wells that record the Cretaceous-Paleogene (K-Pg) boundary. The studied well GEo-02 (purple) is located in Lully area, Geneva, Switzerland (46.159 871° N, 6.067 610° E; WGS84). Map modified from (BRGM, 2003). **(B)** Synthetic log of the GEo-02 well showing lithostratigraphic units from the Upper Jurassic to the Eocene.

2024; Schölderle et al., 2021, 2023, 2025; Zosseder et al., 2022). Although paleokarst features are often out of equilibrium with the current geomorphic setting, they can significantly contribute to aquifer porosity and permeability, and may be reactivated by modern epigenic or hypogenic karstification processes (Goldscheider et al., 2010).

This study characterises the stratigraphy, sedimentology, and diagenesis of the Siderolithic Group in the Geneva Basin, focusing on tectonic and climatic controls on its formation. While primarily geological, the findings also contribute to assessing the geothermal potential of the Siderolithic Group. As part of geothermal exploration, new data from the GEo-02 borehole (SIG, 2020) were analysed, revealing an exceptionally thick interval (up to 158 m) of the Siderolithic Group, challenging previous 2D seismic interpretations and regional geological models (Eruteya et al., 2024). Prior to the drilling of the GEo-02 well, the subject of this study, all boreholes in the Geneva Basin, aimed at hydrocarbon and geothermal energy exploration, encountered only thin siderolithic intervals (0.5 to 6 m; Moscariello, 2019), in contrast to the significantly thicker deposits (up to 20 to 25 m) exposed at Salève Mountain, southeast of Geneva (Charollais et al., 2007, 2023; see Figure 1A).

The term ''siderolithicum'', introduced by Thurmann (1832), is also known as the Bohnerz Formation (Troesch, 1908), lacks a formally defined type section or type locality. Consequently, it does not meet the criteria for formation status and is instead classified as a Group (Menkveld-Gfeller et al., 2016). Generally, it refers to iron-rich, sandy to argillaceous terrestrial rocks first recorded in the Jura Mountains (Renevier, 1877) and the Helvetic Alps (De la Harpe, 1854; Wieland, 1976). In Western Switzerland, siderolithic deposits have been sporadically documented in regional studies (Becker, 2003; Charollais et al., 1994, 1998, 2007, 2013; Collet & Paréjas, 1936a, 1936b; Guglielmetti et al., 2020; Herb, 1988; Jeannottat, 2005; Jenny et al., 1995; Jordi, 1995; Joukowsky & Favre, 1913; Kerrien et al., 1998; Martini, 1962; Mathey, 1976; Moscariello, 2019; Moscariello et al., 2020; Vernet, 1958, 1963; Weidmann, 1984). Similar deposits overlying the Lower Cretaceous unconformity in France (Crozet, 1932; Daniou, 1979, 1981; Debelmas et al., 1961; Delaunay, 1984; Guendon, 1984; Mazenot et al., 1955; Schoeller, 1941; Simon-Coinçon et al., 2000; Thiry & Turland, 1985; Triat, 1982; Triat & Guendon, 1975) indicate a regionally extensive Cretaceous–Paleogene (K–Pg) sedimentary record, characterised by consistent facies and depositional patterns despite lateral discontinuity and sporadic occurrences.

The Siderolithic Group is stratigraphically positioned above a major regional angular unconformity (Figure 1B), which separates the Lower Cretaceous Barremian carbonate platform (c. 122 Ma) from the Oligocene Chattian Molasse (base at c. 28 Ma) (Charollais et al., 2023). This c. 94 Myr hiatus marks major tectonic and climatic shifts that shaped the Cretaceous-Paleogene Boundary through karstification, paleosol formation and siderolithic deposits. The precise geological age of the Siderolithic Group remains uncertain, with limited biostratigraphic evidence suggesting a Lutetian or Bartonian age, based on Eocene marine fossils such as *Nummulites incrassatus* and *Perna lamarcki* reported in Bohnerz-bearing deposits (von Tavel, 1936), and a rodent molar (*cf. Sciuroides* sp.) recovered from a karst infill at Collombey (Weidmann, 1984). However, a re-examination of rodent teeth from quartz-rich sandstone in the Jura foothills, stratigraphically correlated with similar deposits in the Geneva Basin, confirms a Bartonian age (Eocene) based on a diverse and well-preserved micromammal assemblage dominated by theridomyid rodents (Hooker & Weidmann, 2007). This biostratigraphic evidence links deposition to the Middle Eocene Climatic Optimum (MECO), a transient global warming phase marked by intensified weathering and sediment influx (Bohaty & Zachos, 2003; Boscolo Galazzo et al., 2014; Cramwinckel et al., 2018).

2 Geological setting

2.1 Regional framework

The Cretaceous-Paleogene boundary is marked by a sharp unconformity with a stratigraphic hiatus from a passive margin to a continental foreland basin due to the Alpine orogeny (Santonian; Late Cretaceous), driven by the Alpine Tethys subduction and the collision of the European Plate and the Apulian Microplate; and consequently the uplift of the southeast French Massif Central due to the Pyrenean compression during the Late Cretaceous–early Eocene (Olivetti et al., 2020; Séranne et al., 2002). These tectonic processes buckled the lithosphere and induced basin inversion, extending up to 1700 km north of the Alpine and Pyrenean fronts, culminating in the Helvetic Shelf buckling (Pfiffner, 2014; Smeraglia et al., 2021).

At the Paleocene-Eocene transition (PETM, c. 56 Ma), the Alpine foreland compression ceased, while ongoing Pyrenean collision induced flexural bulging toward the northwest (Michard, 2002; Stampfli et al., 1998). This tectonic uplift led to the erosion and karstification of 1000 to 2000 m of Mesozoic limestone (Allen et al., 1991; Schegg & Leu, 1996; Sissingh, 1997), initiating a first phase of paleokarst development. During the Lutetian (c. 45 Ma), flexural subsidence related to foreland basin development affected the Dauphinois and Helvetic shelves, while the associated peripheral bulge provided conditions favourable for continued karstification and subsequent siderolithic deposition (Berger et al., 2005). By the Priabonian (c. 35 Ma), compressional stresses from the Alpine and Pyrenean collision zones intensified and activated the European Cenozoic Rift System (ECRIS), forming the Rhine and Bresse Grabens (Dèzes et al., 2004; Ziegler, 1992). East-west extension in the northern Alpine foreland fragmented the European margin, forming the north-south-oriented Rhine Graben and, in the transfer zone south of the Vosges, the more laterally extensive and structurally complex Bresse Graben (Schumacher, 2002) (Figure 2).

Eocene warm and humid conditions were followed by global cooling event at the Eocene-Oligocene boundary, leading to the onset of Antarctic glaciation (Zachos et al., 2001, 2010). There were intervals of warm and humid conditions, including the PETM (c. 56 Ma), which caused a 4 to 8 °C global temperature rise (Westerhold et al., 2009; Zachos et al., 2003). We propose that the Siderolithic Group was deposited during the Middle Eocene Climatic Optimum (MECO, c. 40 Ma), a transient warming phase (Bohaty et al., 2009; D'Onofrio et al., 2021), marking an unconformity from earlier erosion to active sedimentation. However, sedimentary records of MECO in continental settings remain scarce (El-Fawal et al., 2011; Methner et al., 2016; Peris Cabré et al., 2023; Sharma et al., 2024). Early Eocene volcanic activity, possibly linked to the North Atlantic Igneous Province or Neotethys volcanic arcs

(Pfiffner, 2014), could have been the trigger for the early and middle Eocene warming periods, resulting in intensified weathering and the formation of terra rossa. Similar processes were observed in the Eastern Alps during the early Eocene (Ypresian) (Činčura, 1990; Kázmér et al., 2003; Mindszenty et al., 1988).

In the Geneva Basin, the provenance of the Siderolithic Group is debated. Some suggested in-situ weathering of the local Cretaceous strata (Collet & Paréjas, 1936b), while others proposed a lateritic source from the French Massif Central Triassic unit (Charollais et al., 1988; Conrad & Ducloz, 1977; Deschamps, 1958). Detrital quartz is attributed to the erosion of the Lower Cretaceous or Triassic sandstones of the French Massif Central (Charollais et al., 1988).

2.2 Geneva Basin framework

The Geneva Basin (Figure 1A) is a NE–SW trending Cenozoic basin within the North Alpine Foreland Basin (Chevalier et al., 2010; Moscariello, 2019). It is bounded by the Haute-Chaîne of the Jura Mountains (NW), Vuache Mountain (W), and Salève Mountain (SE) with a significant faults system acting as potential fluid pathways (Clerc & Moscariello, 2020).

The Alpine orogeny uplifted and caused the erosion of Cretaceous sedimentary successions, forming the K-Pg unconformity and intense karstification of Lower Cretaceous carbonates. In the Geneva Basin in Switzerland and neighbouring France, 2D seismic profiles reveal extensive karst features (Eruteya et al., 2024). Bedrock age, ranging from Valanginian to Aptian in the Geneva Basin (Charollais et al., 2007), varies with erosion depth, controlled by European early Cenozoic rifting and Alpine orogeny. Bedrock in the Geneva Basin ranges from the upper Hauterivian–lower Barremian Rochers des Hirondelles to the lower Valanginian Vuache Formation (Charollais et al., 2007; Pictet, 2021; Strasser et al., 2016), with the mid- and upper Cretaceous sections absent. In adjacent basins, younger Cretaceous formations form the bedrock, including the Perte-du-Rhône Formation (Aptian-Cenomanian) in Rumilly (S. Guillaume, 1966; Pictet et al., 2016; Vial et al., 1989), the Narlay Formation (Cenomanian-Coniacian) in Yvoire (Mont-de-Boisy borehole, S. Guillaume, 1966), and equivalent units in the Swiss-French Jura (A. Guillaume & Guillaume, 1969).

In the northern Jura, karst cavities in the eroded bedrock were infilled by the Siderolithic Group, consisting of red clay, quartz sand layers, and ferruginous pisoliths, with a Bartonian age confirmed by rodent teeth (Hooker & Weidmann, 2000, 2007), which correlates with similar deposits on Salève (L'Echelles, Savoie, France) and marine faunas of Paleocene (Selandian) age (Charollais & Wellhauser, 1962).

Following the Siderolithic Group deposition, major hiatuses in the Geneva Basin include a 17 Myr gap marked by the absence of the Lower Marine Molasse (LMM), Upper Marine Molasse (UMM), and Upper Freshwater Molasse (UFM), with only the Chattian-Lower Miocene Lower Freshwater Molasse (LFM) overlying the K-Pg unconformity (Beck et al., 1998). This hiatus is likely linked to the Vuache fault activity (Blondel, 1988), which influenced the Rupelian-Burdigalian paleogeography (Moscariello et al., 2014). Another c. 28 to 25 Myr gap separates the LFM from the overlying Pleistocene glacial deposits, reflecting a prolonged phase of regional uplift associated with Jura tectonics (Miocene–Pliocene) and successive erosional processes, including glacial incision the late Pliocene (Charollais et al., 2007; Haas et al., 2022; Moscariello, 2021).

3 Material and methods

This study focuses on the wire-log data and drill cuttings acquired from the GEo-02 geothermal exploration well drilled near the village of Lully (Canton of Geneva; 46.159 871° N, 6.067 610° E; WGS84) (Figure 1A). The well was spudded in October 2019. Operations stopped when drilling hit the Upper Jurassic (Kimmeridgian–Oxfordian) carbonate units at a depth of 1455.7 m below ground level (bgl) in May 2020.

3.1 Borehole wire-logs

The suite of borehole wire-logs available from the GEo-02 includes Spectral Gamma Ray (GR), Density (DEN), Spontaneous Potential (SP), Caliper (CAL), Sonic (SON), and Resistivity (RES) logs. RES and GR logs are used to distinguish different geological units based on their petrophysical properties, which include characteristics such as lithology, mineralogical composition, diagenesis, and fluid(s) content. Unfortunately, the RES wire-log was not continuously recorded, and two data gaps occur: from 632 to 667 m, and from 792 to 808 m. Furthermore, there has been a change of caliper at 659.5 m and 814.6 m, interfering with the acquisition of gamma ray and resistivity at these depths.

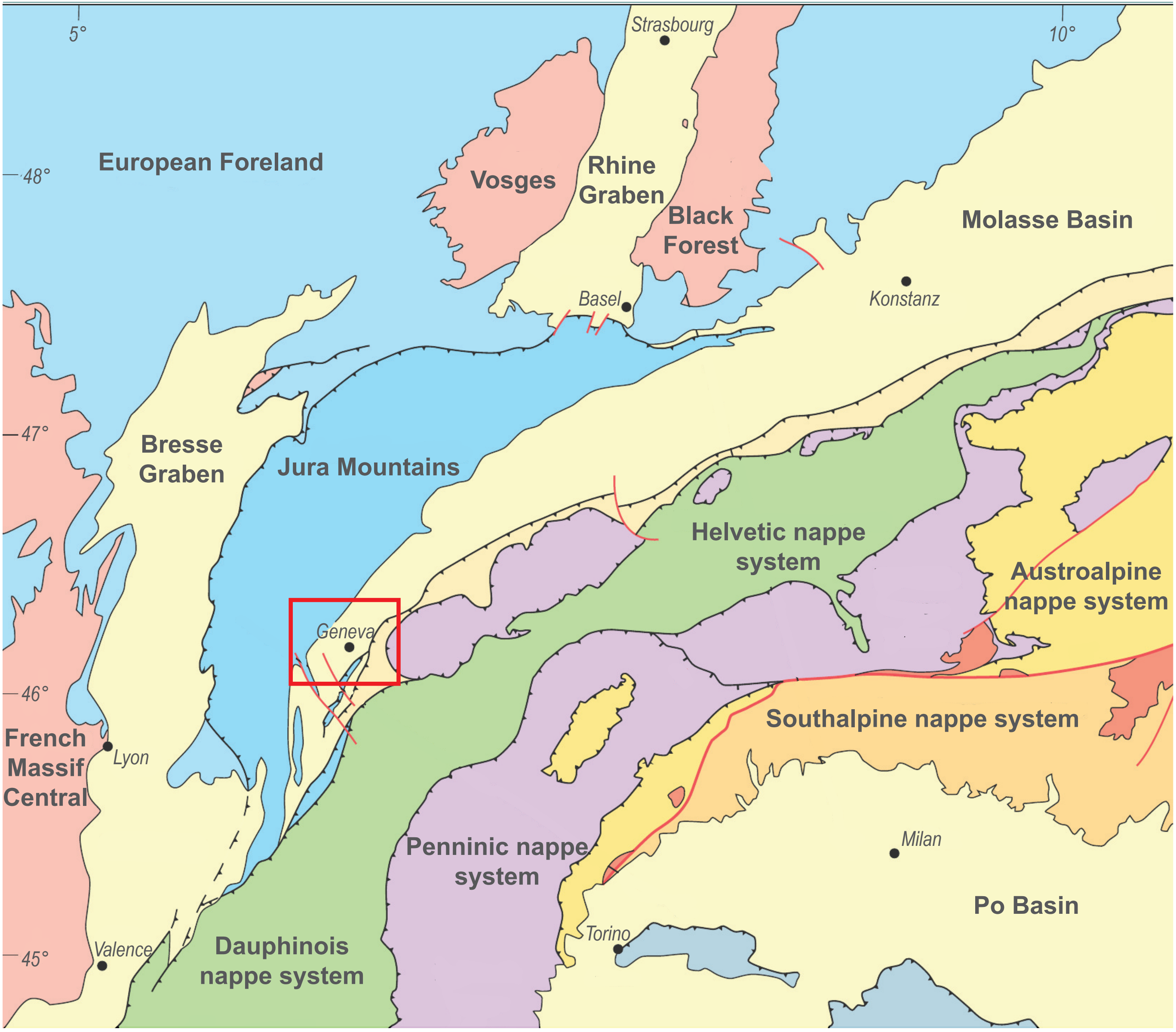

Figure 2 – Present-day tectonic configuration of the northwestern Alpine region, highlighting the Geneva Basin (red box) as the study area. The region lies between the Dauphinois and Helvetic nappe systems, within the broader Alpine foreland. The Rhine Graben (north of the Vosges) and the Bresse Graben (to the west of the Jura Mountains) represent major extensional features of the European Cenozoic Rift System (ECRIS), initiated during the Priabonian (c. 35 Ma) in response to compressional stresses from Alpine and Pyrenean orogenesis. These rift structures reflect the fragmentation of the European margin under east–west extension in the northern Alpine foreland. Modified from Pfiffner (2014).

3.2 Cuttings

Drill cuttings have been sampled over a 454 m thick stratigraphic interval encompassing the lowermost part of the Oligocene Molasse (544 m bgl) to the lowest part of the Lower Cretaceous (998 m bgl) (Figure 3). Samples have been selected every 10 metres at the top, middle, and bottom of each unit or formation, and every 2 m across the transitions between the LFM and the overlying Siderolithic Group, as well as between the Siderolithic Group to the underlying Cretaceous units (Figure 3). Inefficient mud circulation or caving could compromise the representativeness of the cuttings due to pollution from drilling mud and the mixing of cuttings from different stratigraphic intervals. To avoid these issues, the siderolithic cuttings have been washed with distilled water and then dried at 30 °C. The samples have also been examined with a binocular microscope to hand-pick and remove all alien components such as younger units (i.e., Molasse sandstone or carbonates) and debris from drilling operations (metal fragments). To determine the facies according to depth, the proportion of cuttings with a predominant lithology is considered with a minimum error margin of 2 m.

Following this preparation, 63 samples were selected for thin sections and quantitative evaluation of

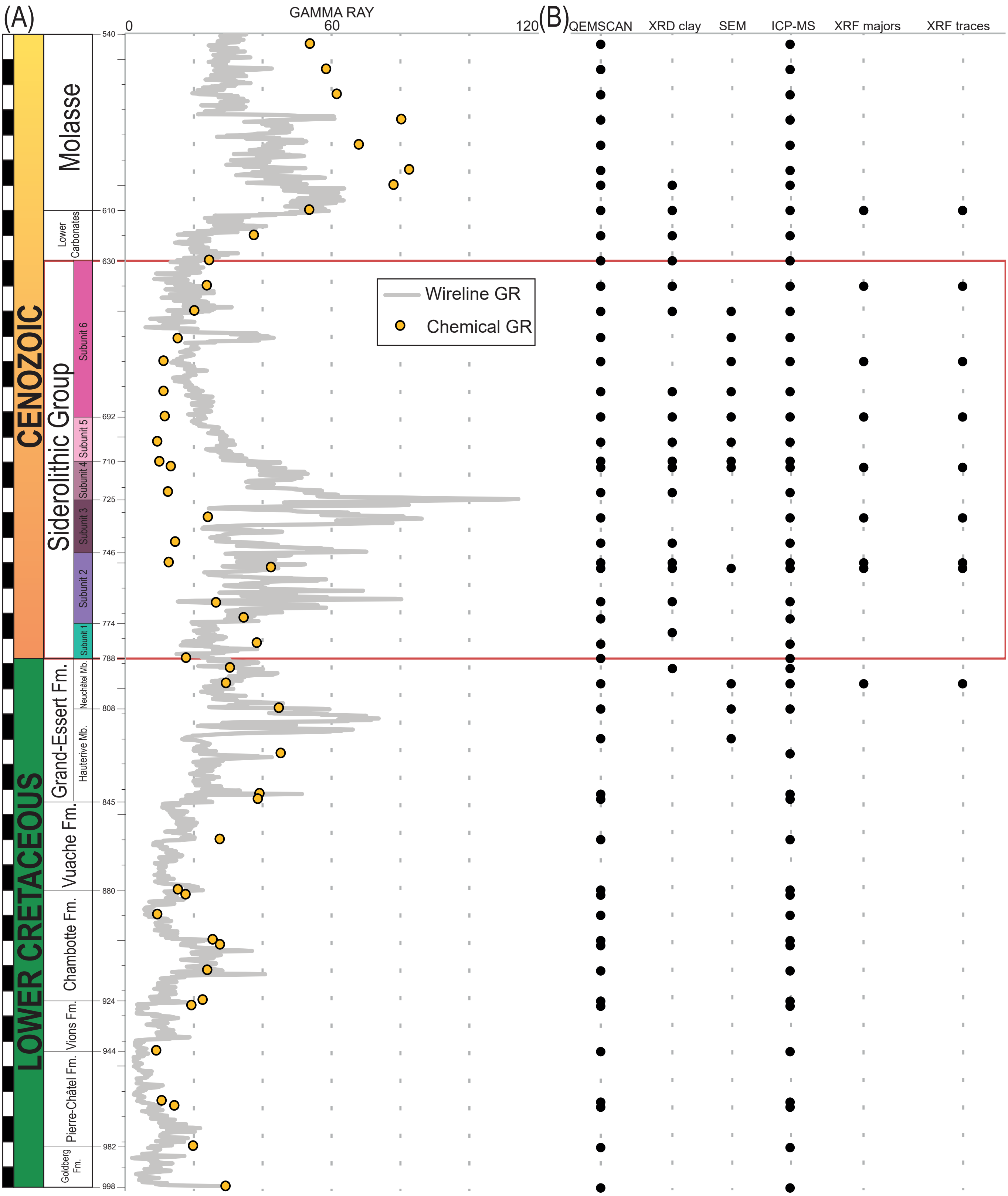

Figure 3 – Stratigraphic log of the GEo-02 well. **(A)** Comparison of wireline gamma ray (grey curve) and chemical gamma ray values (yellow dots) derived from ICP-MS measurements. **(B)** Sample distribution for QEMSCAN, XRD (clay), SEM, ICP-MS, and XRF (major and trace elements). The red box outlines a karst infill interval associated with elevated gamma ray values in the lower part of the Siderolithic Group, which is not entirely composed of karst deposits.

minerals by scanning electron microscopy (QEMSCAN) analysis, 48 for ultra-trace inductively coupled plasma - emission spectrometer/mass spectrometry (ICP-ES/MS), 9 for X-ray fluorescence (XRF), and 18 for X-ray diffraction (XRD) clay fraction analysis.

3.2.1 Petrography and mineralogy

The top Cretaceous bedrock of the K–Pg sequence in the GEo-02 borehole was sampled from 808 to 788 m bgl.

Petrographic investigations involve the analysis of 63 polished thin sections made from cuttings larger than 250 μm in diameter to obtain grain and cement texture data (Figure 3). Thin sections were carbon-coated for QEMSCAN analysis to quantify the mineralogical content using a FEI QEMSCAN Quanta 650F at the University of Geneva. Scanning resolution was 20 μm. The QEMSCAN modal mineralogy data were integrated with rock petrography to assess the stratigraphical control over the mineralogical distribution, including clay minerals and cement.

The clay fraction (< 2 μm fraction) was separated using ultrasonic dispersion and centrifugation. Oriented mounts were analysed in air-dried conditions using a PANalytical Empyrean diffractometer (Cu-Kα, λ = 154.06 pm) at the University of Geneva. Diffractograms were converted to d-spacing using Bragg's Law (Bragg, 1913). Clay minerals were identified by diagnostic basal reflections, and their relative abundances (smectite, illite, kaolinite, chlorite) estimated from peak intensities (Figure 4).

3.2.2 Geochemistry

XRF was performed on nine powder samples using a Philips PW 1410/00 spectrometer, equipped with a Cu-Kα radiation source, a Rhodium tube and LiF (200) at the University of Lausanne to determine bulk chemical composition, mercury (Hg) and Loss on Ignition (LOI) contents. Samples for XRF analysis were powdered using a tungsten mill, resulting in overestimated W values in the data; therefore, W values from XRF analyses are excluded. LOI determines the percentage of weight loss of a sample when subjected to high temperature. It represents the combined loss of volatile components, such as water, carbon dioxide, and organic matter.

ICP-ES/MS was used for bulk rock inorganic geochemistry at Bureau Veritas (Canada, Vancouver). Forty-eight samples of 0.25 g have been heated in HNO_3, $HClO_4$, and HF to fuming, followed by drying. The residual material was then dissolved in HCl. Fifty-nine elements among major, trace, and rare elements were measured. The rare earth elements (REE) were further divided to light REE (LREE; atomic masses < 153: La, Ce, Pr, Nd, Sm, and Eu) and heavy REE (HREE; atomic masses > 153: Gd, Tb, Dy, Ho, Er, Tm, Yb, and Lu) based on their atomic masses. Partial digestion occurs for certain minerals and oxides of Cr and Ba, as well as Al, Fe, Mn, Sn, Ta, and Zr. Volatilisation during fuming may have resulted in loss of As, S, Se, and Sb content.

The chemical index of alteration (CIA) is widely used to determine the degree of chemical weathering. CIA is calculated using the following formula (Nesbitt & Young, 1982):

$$CIA = \left[\frac{Al_2O_3}{Al_2O_3 + CaO^* + Na_2O + K_2O}\right] \times 100 \qquad (1)$$

where CaO* is the CaO associated with the silicate fraction.

ICP-MS geochemistry data were used to create a synthetic chemical gamma ray curve to control its reliability with the wireline Gamma Ray measurements (Figure 3A). The chemical gamma ray curve calculations were developed specifically for geochemical logging and integrated as a depth-matched composite log using the following equation from Schweitzer et al. (1988):

$$\text{Chemical GR} = 16.32 \cdot K + 8.09 \cdot U + 3.93 \cdot Th \qquad (2)$$

The raw ICP-MS geochemical data served as input for this model.

4 Results

Petrographic, mineralogical, geochemical, and petrophysical analyses of the GEo-02 well (summarised in Table 1) reveal a sharp lithological and compositional contrast across the K-Pg unconformity. This major discontinuity separates the karstified marine carbonate platform from an overlying sedimentary succession composed of fluvial, lacustrine, and aeolian deposits of the Siderolithic Group, overlain by lacustrine carbonates and the siliciclastic LFM.

4.1 Carbonate bedrock (808 to 788 m bgl)

The carbonate bedrock consists of bioclastic echinodermal limestone with packstone and grainstone textures. Components include bryozoans, corallinaceous

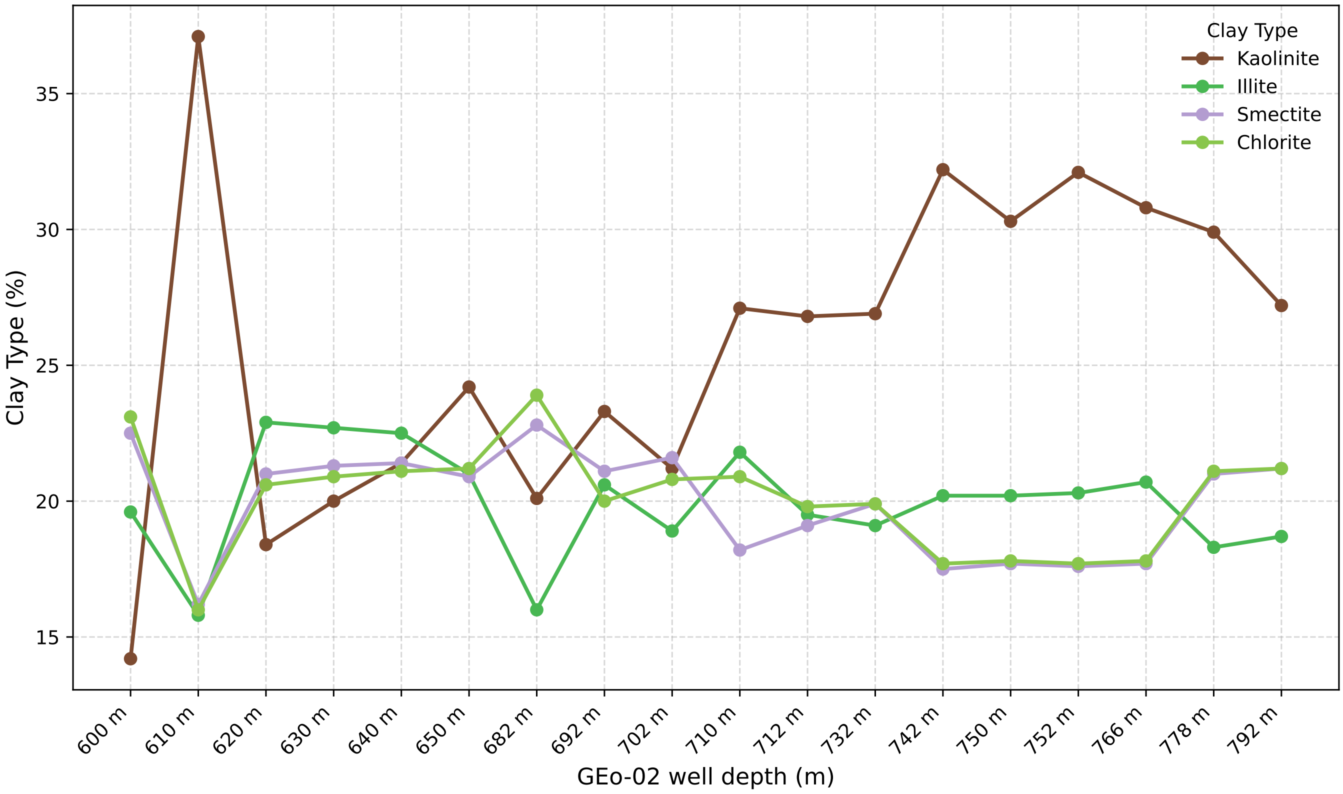

Figure 4 – Clay mineral composition (%) with depth in well GEo-02, based on XRD analysis of the < 2 µm fraction. Relative abundances of kaolinite, illite, smectite, and chlorite were estimated from diagnostic peak intensities in air-dried samples.

algae, dasycladales, fine angular detrital quartz, and glauconite. Siderite within micrite is also observed at 802 m.

4.2 Six subunits of the Siderolithic Group

The Siderolithic Group (788 to 630 m bgl) is characterised by abundant quartz content (QEMSCAN), elevated gamma ray signals indicating clay enrichment, and high CIA values indicating intense chemical weathering. Subunit 1 shows elevated CaO, LOI, Fe-oxides and kaolinite. Upward, CaO, LOI, Fe-oxide, kaolinite, and CIA values progressively decrease, while quartz content increases. Sr trends align with CaO, reflecting carbonate remobilisation. Table 1 summarises the petrophysical, mineralogical, and geochemical trends across the six subunits.

4.2.1 Subunit 1 (788 to 774 m bgl)

QEMSCAN indicates an increased proportion of detrital quartz (≈ 51.95 wt%) associated with a bioclastic echinoderm limestone (Figure 5A). XRD at 778 m bgl confirms the presence of kaolinite, chlorite, and illite (Figure 4). Geochemical measurements show high LOI, elevated Fe-oxides, and elevated Mn (269.5 ppm) and Sr (161.5 ppm) concentrations. Wireline data reveal low gamma ray and high resistivity (253 Ω m). Hg concentrations are low. These data suggest the development of a paleosol horizon formed atop carbonate bedrock. Reflecting subaerial exposure and pedogenic overprinting.

4.2.2 Subunit 2 (774 to 746 m bgl)

This interval consists of quartz-rich sandstone (82.49 wt%) with associated kaolinite, glauconite (Figure 5F), and dolomite-apatite phases (Figure 5G and H). XRD at 766 m and 752 m identifies kaolinite, chlorite, and illite (Figure 4). Gamma ray values increase from 19.22 to 38.65 API, while resistivity decreases to 120 Ω m. LOI declines to 6.65 wt%. Hg reaches its hights measured value (111.2 ppm) in this interval, with Mn concentrations also elevated (443.25 ppm). This subunit marks a transition from the paleosol horizon of subunit 1 to siliciclastic-dominated deposition.

4.2.3 Subunit 3 (746 to 725 m bgl)

This unit is characterised by high gamma ray values (113.95 API) and low LOI (2.85 wt%), indicating a clay-rich sandstone. Quartz content is high (90.97 wt%), and XRD confirms a matrix dominated by kaolinite, chlorite, and illite, with siderite also present (Figure 6A and B). Resistivity remains stable at 120 Ω m. CIA values range from 49.9 to 63.8 %, and peak Mn (567.5 ppm) is accompanied by elevated Hg (77.4 ppm). The mineralogical and geochemical signatures reflect a mature, quartz-rich sandstone with significant clay input and continued chemical weathering of feldspar.

4.2.4 Subunit 4 (725 to 710 m bgl)

This interval is dominated by quartz (94.11 wt%), with minor kaolinite, chlorite, and siderite identified by XRD and QEMSCAN (Figure 6C–F). Gamma ray values are stable (≈ 45 API), LOI is reduced (1.95 wt%), and Sr concentrations are low. CIA values range from 6 to 60 %. Mn declines to 46.64 ppm, while Hg remains elevated at 86 ppm. These characteristics reflect a mature, well-sorted sandstone with minimal clay and carbonate content.

4.2.5 Subunit 5 (710 to 692 m bgl)

Quartz content peaks at 96.25 wt%, with XRD and QEMSCAN analyses confirming only minor amounts of kaolinite and chlorite. Gamma ray values are low (33 to 23 API), and the sandstone is composed of coarse, well-rounded quartz grains with minimal clay retention (Figure 7A and B). Hg and Mn concentrations decrease to 18.5 to 19.5 ppm and 42 ppm, respectively, alongside Sr depletion.

4.2.6 Subunit 6 (692 to 630 m bgl)

Quartz makes up 91.04 wt% of this interval, with coarse grains embedded in an illite-rich siltstone matrix (Figure 7D and F). XRD identifies kaolinite, chlorite, illite, and serpentine. Geochemical data show increasing concentrations of Ba, K_2O, Na_2O, and MgO. Mn is elevated at 122.15 ppm, and Hg ranges from 45 to 84.6 ppm. These features indicate a continued siliciclastic system with increasing influence from the overlying Molasse, as evidenced by serpentine and enriched alkali and alkaline earth elements.

4.3 Overlying Units

4.4 Lacustrine Carbonates (630 to 610 m bgl)

Petrographic and mineralogical analyses reveal three distinct lithologies: carbonate mudstone (31.88 wt% calcite, 4.58 wt% dolomite), illite-rich clay, and sandstone containing quartz (26.30 wt%), micas, chlorite, plagioclase, and serpentine. XRD confirms the presence of illite, chlorite, and serpentine in association with both carbonate and siliciclastic components. Geochemical data show elevated Sr (280 ppm), moderate LOI (10.50 wt%), high SiO_2 (60.10 wt%) and Al_2O_3 (8.93 wt%). Mn is high (632 ppm), and Hg is low (9.8 ppm). The gamma ray correlation between ICP-MS and wireline data is moderate (R^2 = 0.562), indicating potential discrepancies in geochemical and cuttings data for this interval. The combined carbonate and siliciclastic mineralogy, along with elevated Sr and moderate LOI, suggests deposition in a lacustrine setting with some organic matter input. High Mn implies redox-sensitive diagenesis. Low Hg values further indicate a limited volcanic contribution to this interval. However, the occurrence of serpentine, likely derived from the overlying Molasse, together with discrepancies between geochemical and cuttings data, complicates stratigraphic attribution. Additional analyses are therefore required to resolve if this unit should be assigned to the Siderolithic Group.

4.5 Lower Freshwater Molasse (LFM) (610 to 46 m bgl)

Petrographic and mineralogical analyses show illite-rich clay and sandstone composed of quartz (26.87 wt%), micas, chlorite, plagioclase, and serpentine. XRD confirms kaolinite, chlorite, and illite, along with a distinct serpentine (chrysotile) peak. Geochemical data reveal high SiO_2 (50.58 wt%) and Al_2O_3 (10.66 wt%), elevated Mn (669.14 ppm), and strong Sr (335.57 ppm) and Ba (218.71 ppm) concentrations. Gamma ray data show a strong gamma ray correlation between ICP-MS and wireline values (R^2 = 0.8633). Trace element data include Cr (178 ppm), Ni (151.79 ppm), and an LREE/HREE ratio of 8.14. These characteristics indicate a siliciclastic-dominated fluvial system with significant detrital input, including serpentine likely sourced from ultramafic rocks in the Alpine front. The high Mn content reflects redox-sensitive diagenesis, while elevated Sr and Ba suggest the presence of detrital carbonate phases rather than lacustrine precipitation

5 Discussion

The sedimentary and diagenetic evolution of the Siderolithic Group in GEo-02 is shaped by structural controls, climate-enhanced karstification, sediment transport, and post-depositional diagenesis. This discussion integrates these factors to explain karst formation, sediment trapping, diagenetic overprint, and reservoir implications.

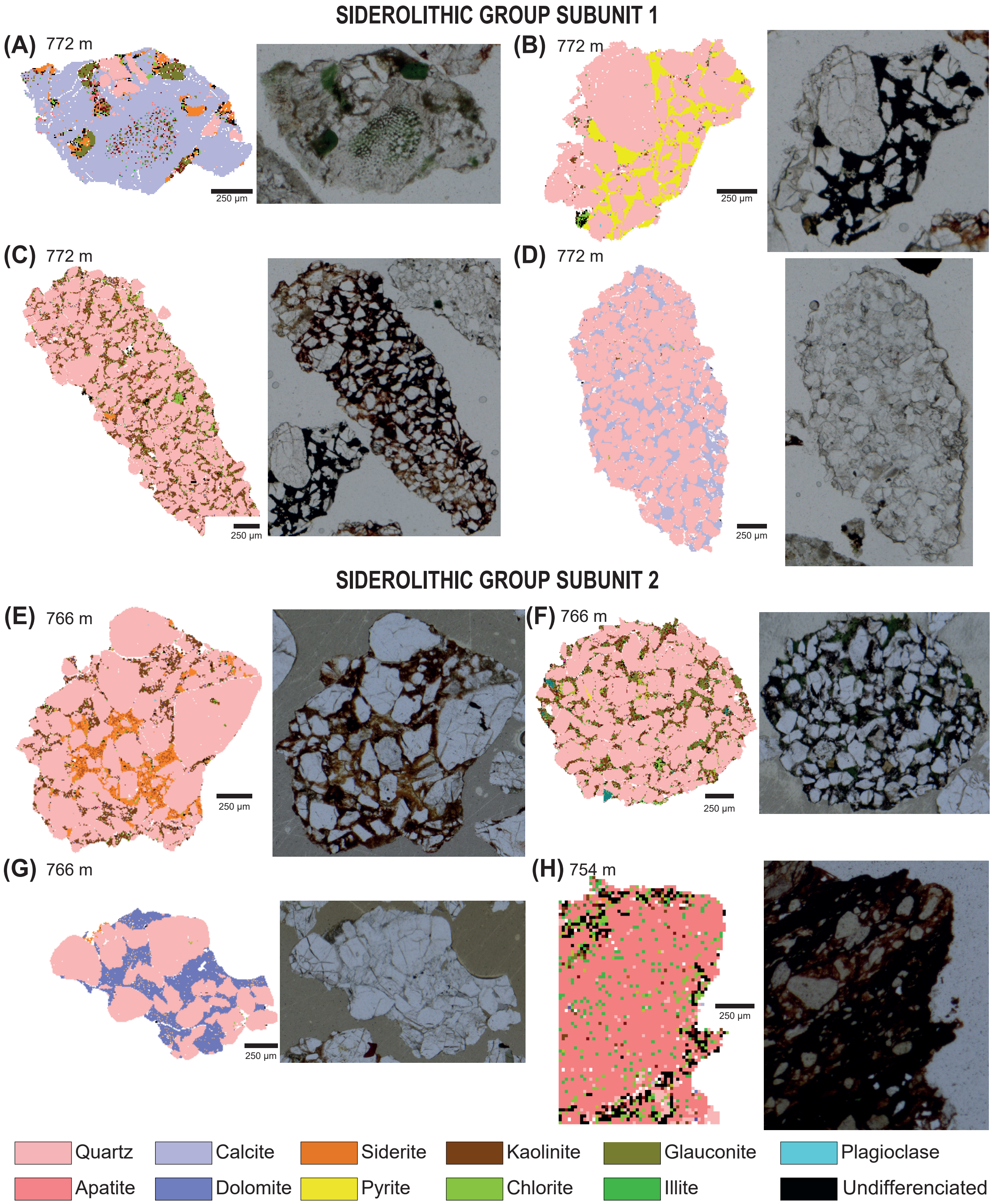

Figure 5 – QEMSCAN images and optical photomicrographs of Siderolithic subunits 1 and 2. **(A)** Carbonate with glauconite grains, echinoderms and siderite. **(B)** Sandstone with variable size and roundness of quartz grains in a pyritic matrix. **(C)** Sandstone with variable matrix (chlorite, kaolinite, siderite). **(D)** Fine sandstone with calcitic cement. **(E)** Sandstone with siderite cement and kaolinite matrix. **(F)** Sandstone with glauconite and rutile grains in a kaolinite matrix. **(G)** Sandstone with dolomitic cement. **(H)** Siltstone with apatite matrix.

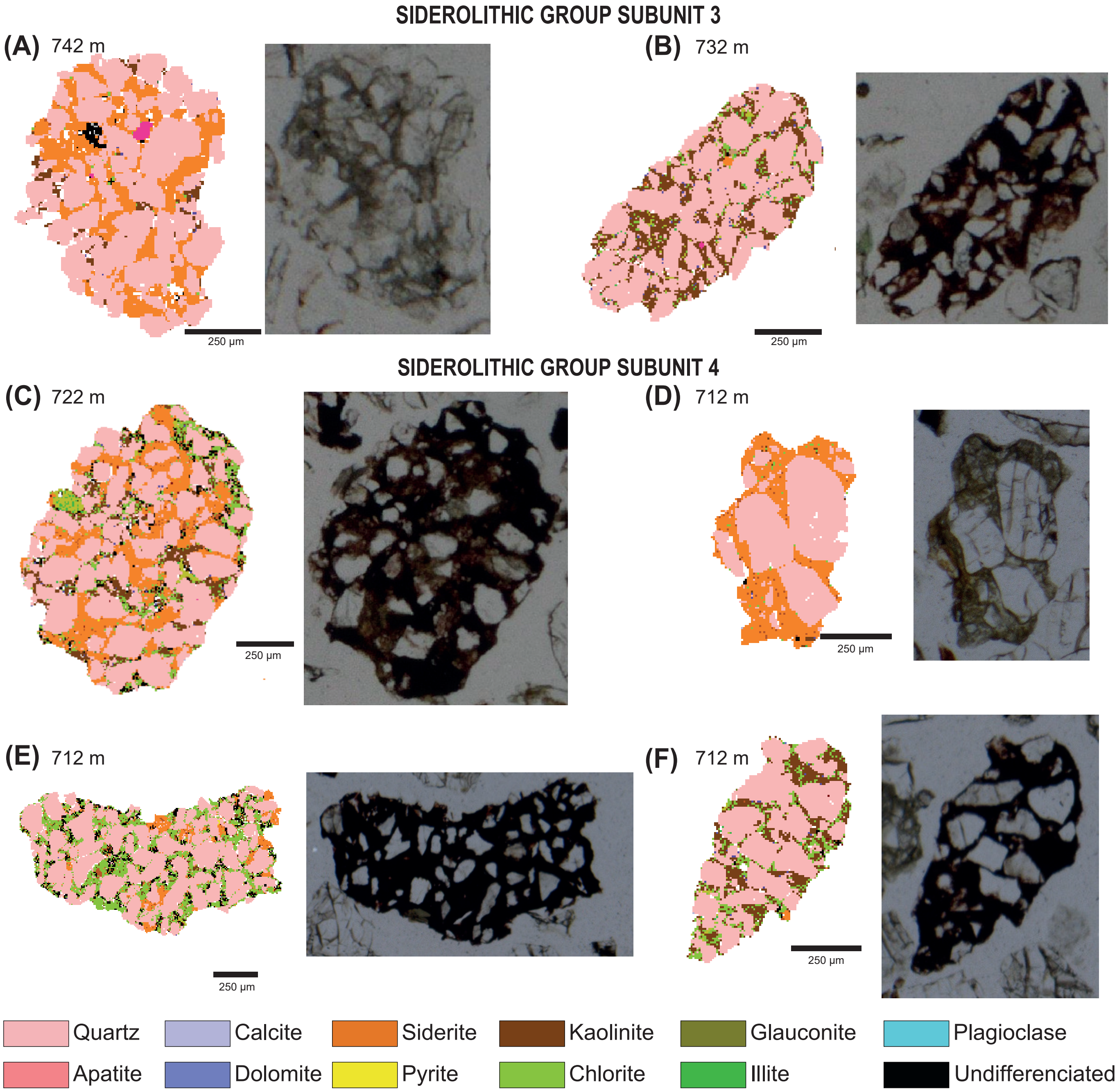

Figure 6 – QEMSCAN images and optical photomicrographs of Siderolithic subunits 3 and 4. **(A)** Fine sandstone with a siderite cement. **(B)** Fine sandstone into a chlorite and kaolinite matrix. **(C)** Fine sandstone into a siderite cement and chlorite-kaolinite matrix. **(D)** Medium sandstone with a siderite cement. **(E)** Fine to very fine sandstone with a predominant chloritic matrix with some spots associated to the siderite cement. **(F)** Fine sandstone with a chlorite and kaolinite matrix.

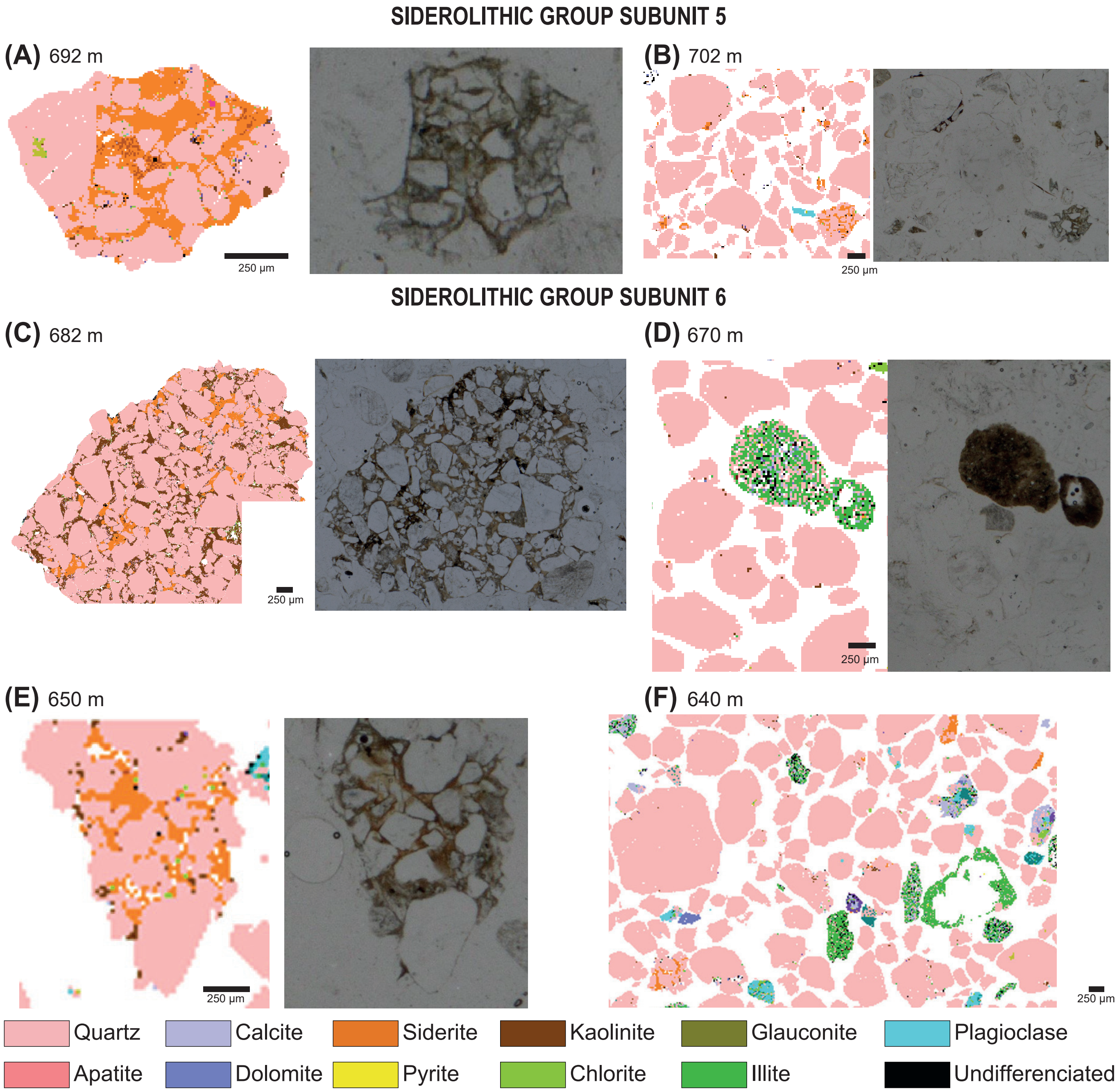

Figure 7 – QEMSCAN images and optical photomicrographs of Siderolithic subunits 5 and 6. **(A)** Sandstone with a bimodal distribution of fine subangular quartz grains with coarse to very coarse rounded quartz grains with siderite cement. **(B)** Coarse sandstone and rounded quartz grains. **(C)** Coarse sandstone with siderite cement and kaolinite matrix. **(D)** Coarse and rounded quartz grains, with a cutting of illite-rich clay. **(E)** Sandstone with a bimodal distribution of fine subangular quartz grains with coarse to very coarse rounded quartz grains with siderite cement. **(F)** Coarse and rounded quartz grains, with illite-rich clay cutting, and a microcrystalline cutting with felspar, plagioclase and serpentinite.

Stratigraphy	Depth	Thickness	Lithology and Texture	Main Minerals	Quartz Grain Size and Shape	Clay Analysis	Major Oxides		LOI	CIA	Trace Elements		Hg	LREE / HREE	Gamma-Ray	Resistivity	Number of Samples (n)
	(m bgl)	(m)					(≥ 5 %)	(< 5 %)	(%)	(%)	(≥ 60 ppm)	(< 60 ppm)	(ppm)		(API)	(Ω m)	
Lower Freshwater Molasse (LFM)	> 610	66	Illite clay & sandstone	Quartz (26.87 %), Illite (17.66 %), Calcite (16.80 %), Dolomite, Chlorite	Fine-grained	Kaolinite, chlorite, illite, serpentine	SiO_2 (50.58 %), CaO (11.76 %), Al_2O_3 (10.66 %)	Fe_2O_3 (4.34 %), MgO (3.74 %), K_2O (2.07 %)	2.66		Mn (669 ppm), Sr (335 ppm), Ba (218 ppm), Cr (178 ppm), Ni (151 ppm), Rb (92.03 ppm)		N/A	8.14	37 (average)	24	QEMSCAN (7), XRD (1), ICP-MS (6), XRF (0)
Lacustrine Carbonates	630 to 610	20	Carbonate mudstone	Calcite (31.88 %), Quartz (26.30 %), Illite (9.07 %), Dolomite, Plagioclase	Absent	Kaolinite, chlorite, illite, serpentine	SiO_2 (60.10 %), CaO (11.24 %), Al_2O_3 (8.93 %)	Fe_2O_3 (3.16 %), MgO (4.42 %), K_2O (1.78 %)	10.5		Mn (632 ppm), Sr (280 ppm), Ba (239 ppm), Cr (159 ppm), Ni (161 ppm)	V (51.50 ppm)	9.8	7.38	37 (average)	N/A	QEMSCAN (2), XRD (2), ICP-MS (2), XRF (1)
Siderolithic Group, *Subunit* 6	692 to 630	62	Coarse sandstone with illitic matrix	Quartz (91.04 %), Illite (1.89 %), Calcite (2.22 %), Feldspars	Very coarse	Kaolinite, chlorite, illite, serpentine	SiO_2 (90.32 %)		6.65	25.5 to 35.5	Mn (122 ppm), Ba (72 ppm), Sr (63 ppm)	Ba (55 ppm), V (35.5 ppm), Zn (33 ppm)	45 to 84.6	13.28	19.22 to 38.65 (gradual increase)	Variable	QEMSCAN (7), XRD (5), ICP-MS (7), XRF (3)
Siderolithic Group, *Subunit* 5	710 to 692	18	Super-mature quartz sandstone	Quartz (96.25 %), Siderite (2 %), Traces of kaolinite	Coarse, subrounded	Kaolinite, chlorite, illite	SiO_2 (94.59 %)	Fe_2O_3 (1.90 %)	1.95	46.5 to 56.5		Mn (42 ppm)	N/A	18.12	33 to 23 (decreasing)	120	QEMSCAN (2), XRD (2), ICP-MS (3), XRF (0)
Siderolithic Group, *Subunit* 4	725 to 710	15	Fine sandstone	Quartz (94.11 %), Siderite (2.61 %), Traces of kaolinite & chlorite	Angular-rounded	Kaolinite, chlorite, illite	SiO_2 (93.41 %)	Fe_2O_3 (2.55 %), Al_2O_3 (1.34 %)	1.95	6 to 60	Sr (60 ppm)	Mn (50 ppm), Ba (45 ppm)	86	15.51	≈ 45 (stable)	120	QEMSCAN (2), XRD (1), ICP-MS (3), XRF (1)
Siderolithic Group, *Subunit* 3	746 to 725	21	Fine sandstone with kaolinite/siderite	Quartz (92.07 %), Siderite (4.52 %), Kaolinite (< 1 %)	Angular-subrounded	Kaolinite, chlorite, illite	SiO_2 (80.83 %), CaO (6.28 %)	Fe_2O_3 (3.03 %), Al_2O_3 (2.22 %)	21.55	49.9 to 63.8	Mn (443.2 ppm), Sr (95.7 ppm)	Ba (55 ppm), V (35.5 ppm)	77.4	8.01	113.95 (peak at 725 m)	120	QEMSCAN (3), XRD (2), ICP-MS (3), XRF (1)
Siderolithic Group, *Subunit* 2	774 to 746	28	Fine sandstone	Quartz (82.49 %), Kaolinite (3.74 %), Siderite (2.88 %), Chlorite (1.46 %)	Fine to coarse, rounded	Kaolinite, chlorite, illite, K-feldspar	SiO_2 (46.68 %), CaO (24.32 %)		26.2	6.1 to 66.2	Mn (269.5 ppm), Sr (161.5 ppm)	V (42.50 ppm), Ba (42 ppm)	17.6 to 111.2	10.98	19.22 to 38.65	120	QEMSCAN (8), XRD (3), ICP-MS (4), XRF (2)
Siderolithic Group, *Subunit* 1	788 to 774	14	Pedogenic horizon	Quartz (51.95 %), Calcite (21.27 %), Kaolinite (6.56 %), Fe-oxides, glauconite	150 to 200 µm, subangular	Kaolinite, chlorite, illite	SiO_2 (36.12 %), CaO (29.20 %)	Al_2O_3 (2.95 %), Fe_2O_3 (2.42 %)	N/A	6 to 12	Sr (282 ppm), Mn (278 ppm)	Ba (49 ppm), V (42 ppm)	N/A	9.4	N/A	253	QEMSCAN (4), XRD (1), ICP-MS (5), XRF (0)
Top Carbonate Bedrock	808 to 788	20	Bioclastic echinodermal limestone	Calcite (53.12 %), Quartz (36.18 %), Traces of illite, kaolinite, glauconite, pyrite, apatite	Detrital quartz ≈100 µm	Kaolinite, chlorite, illite	SiO_2 (36.12 %), CaO (29.20 %)	Al_2O_3 (2.95 %), Fe_2O_3 (2.42 %)	N/A		Sr (282 ppm), Mn (278 ppm)	Ba (49 ppm), V (42 ppm)	8.4	9.83	19.22 to 38.65	69	QEMSCAN (8), XRD (1), ICP-MS (6), XRF (1)

Table 1 – Summary of lithological, mineralogical, geochemical, and petrophysical characteristics of the stratigraphic units identified in the GEo-02 borehole (Geneva Basin). The table includes depth intervals, lithology, texture, quartz grain size and shape, dominant clay minerals, major oxides, loss on ignition (LOI), trace element concentrations, mercury content, LREE/HREE ratios, gamma-ray values, resistivity, and the number of analytical samples by method (QEMSCAN, XRD, ICP-MS, XRF). These data support the subdivision of the Siderolithic Group into six distinct subunits and highlight compositional trends from the carbonate bedrock through the siderolithic infill to the overlying Molasse deposits

5.1 Structural and climatic controls on karst development

5.1.1 Fault-controlled karst development in the European Cenozoic Rift System (ECRIS)

The Siderolithic Group in the GEo-02 borehole is exceptionally thick (158 m) compared to others in the Geneva Basin (GEX and CERN wells, except GEX-5), where the Siderolithic Group is much thinner (< 10 m) (Charollais et al., 2007; Moscariello, 2019). The 2D seismic interpretation calibrated with GEo-02, reveals a fault-controlled karst system at the K-Pg boundary (Eruteya et al., 2024), where extensional faulting created the accommodation space later modified by karst processes. The spatial correlation between GEX-5 and GEo-02, both located near NE–SW extensional faults (Clerc & Moscariello, 2020), suggests that faulting influenced the development and preservation of the thick Siderolithic Group deposits through the creation of localised accommodation space.

The opening of the Rhine and Bresse Grabens, part of the broader ECRIS (Dèzes et al., 2004; Ziegler, 1992), likely induced NE–SW normal faulting in the Geneva Basin, increasing fracture density and enhancing groundwater circulation, meteoric water infiltration, carbonate dissolution, deep karstification, and sediment trapping (Agosta et al., 2010; Matonti et al., 2012).

Comparable fault-controlled collapse features have been documented in the Rumilly Basin and Salève Mountain, such as 'La Grande Gorge' and 'La Petite Gorge' (Charollais et al., 2023; Eruteya et al., 2024; Joukowsky & Favre, 1913; Kerrien et al., 1998; Lombard, 1965), where karstified zones and faults intersected, although they do not represent visible or infilled paleokarsts. These structures serve as direct analogues for the subsurface setting at Geo-02, where fault-induced subsidence created accommodation space later affected by climate-driven karstification. Subsequent infill by the Siderolithic Group, followed by lacustrine carbonates and the LFM (Charollais et al., 2007), transformed the karst system into a buried paleokarst.

5.1.2 Climate-driven epigenic karstification and weathering

The GEo-02 Siderolithic Group karst system was significantly influenced by humid Paleocene-Eocene conditions, which enhanced meteoric dissolution, sinkhole formation, and cavity enlargement (Greenwood & Wing, 1995; Moore & Wade, 2013; Pepe & Parise, 2014; Waltham & Fookes, 2003). The presence of paleosols, lateritic profiles, and terra rossa at the karst interface reflects post-karst processes, specifically prolonged subaerial exposure and intense tropical weathering following karstification (Bautista et al., 2011; Durn, 2003).

Geochemical evidence confirms paleosol development in the lower Siderolithic Group subunits, with high LREE concentrations (24 to 119 ppm) in subunits 1–2, decreasing in subunit 3 (Figure 8), indicating a progressive decline in pedogenic influence (Durn et al., 2021). The red coloration of the cuttings (788 to 710 m bgl, subunits 1–4) and high LOI in subunit 1 are characteristic of iron-rich paleosols (terra rossa) formed under warm, humid conditions (Boero & Schwertmann, 1989; Durn, 2003).

The high Fe, Mn, V, and Co concentrations of subunits 1–3 (Figure 8), reflect intense weathering and prolonged subaerial exposure. Lateritic weathering and Fe-Mn mobilisation are particularly evident in these subunits, where Fe-oxides (46.68 wt%), LOI (21.55 wt%), Mn (269.5 to 443.25 ppm), and Al_2O_3 (6.28 wt%) indicate strong leaching and chemical alteration (Bárdossy, 1982; Mongelli et al., 2014; Tućan, 1912). Mn and Ba enrichment further suggests a tropical karst landscape with significant hydrochemical alteration (Micheletti et al., 2023).

The presence of kaolinite, identified by characteristic XRD peaks and through QEMSCAN (Figure 9), likely formed from plagioclase and K-feldspar alteration (Banfield & Eggleton, 1990; Meunier, 2005) or from terra rossa-type soils (Durn et al., 1999). CIA values in subunits 2–4 indicate low to moderate weathering intensity (Figure 10A), supporting the hypothesis that kaolinite formation was climatically controlled (Fernández-Caliani et al., 2010).

The presence of terra rossa overlying the karst surface indicates a prolonged period of subaerial exposure, possibly linked to the Cenomanian unconformity that affected carbonate platforms across the western Tethys (Morsilli et al., 2017). This aligns with regional uplift and exposure of Lower Cretaceous and Jurassic limestones, followed by karstification and infill. The humid tropical to subtropical conditions of the Eocene likely favoured lateritic weathering and paleosol formation, as observed in the Pannonian Basin,

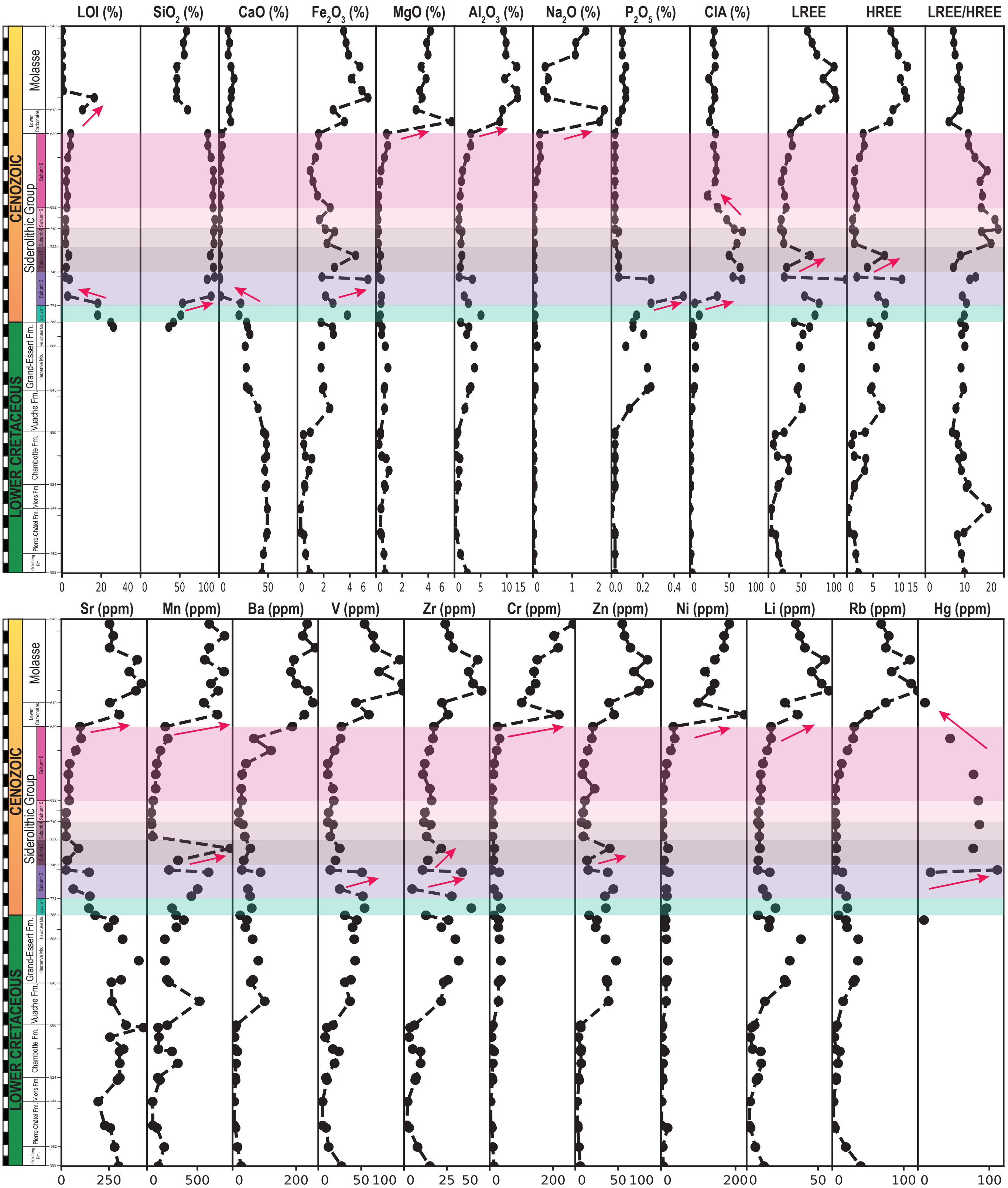

Figure 8 – Chemostratigraphy of the Cretaceous-Paleogene (K-Pg) boundary of the GEo-02 well from ICP-MS and XRF data. **(A)** LOI, major oxides, CIA, and rare earth elements. **(B)** Trace elements

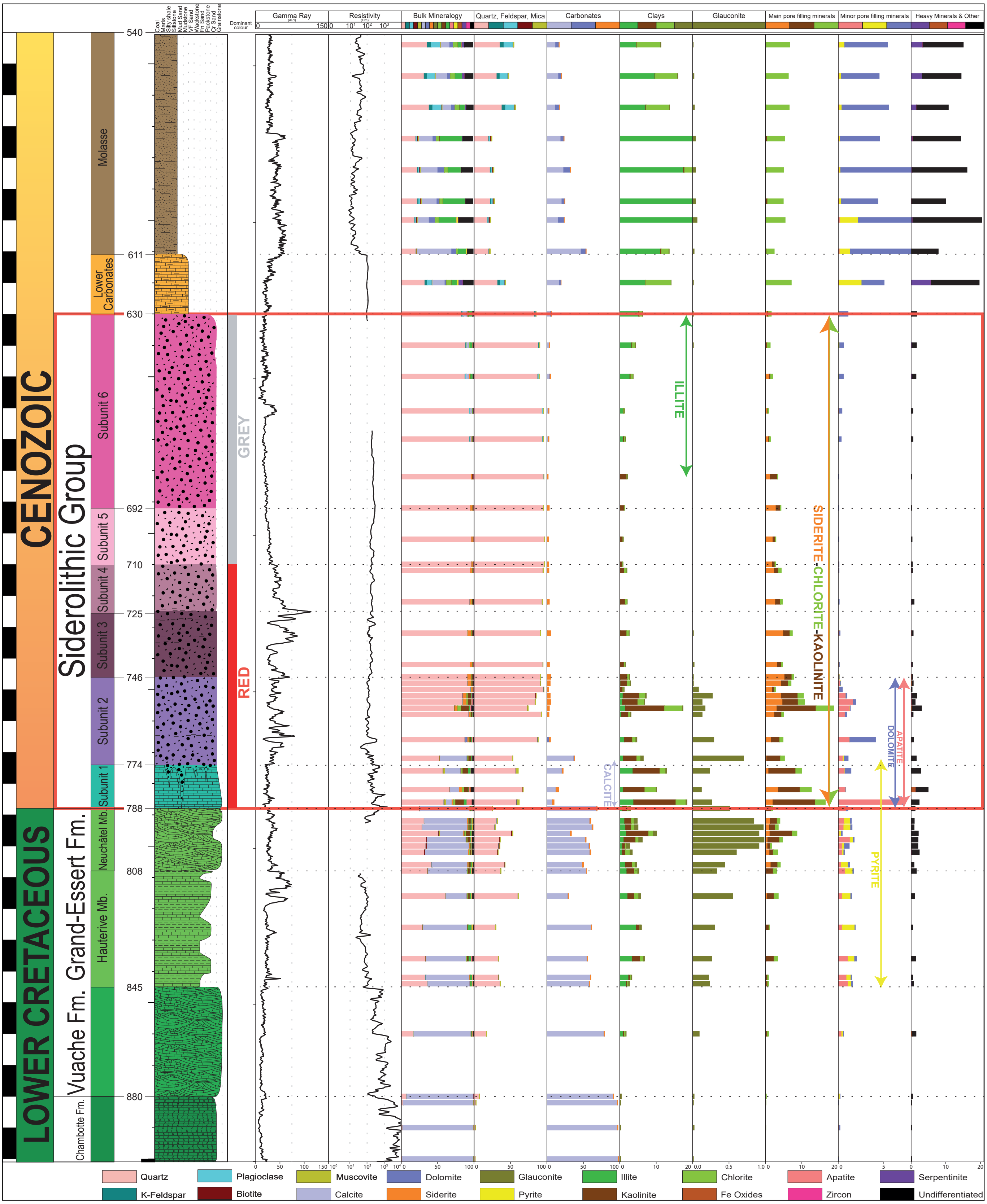

Figure 9 – Correlation of the Cretaceous-Paleogene (K-Pg) boundary of the GEo-02 well based on geophysical data (Gamma Ray and Resistivity) and mineralogical quantification obtained from QEMSCAN analyses.

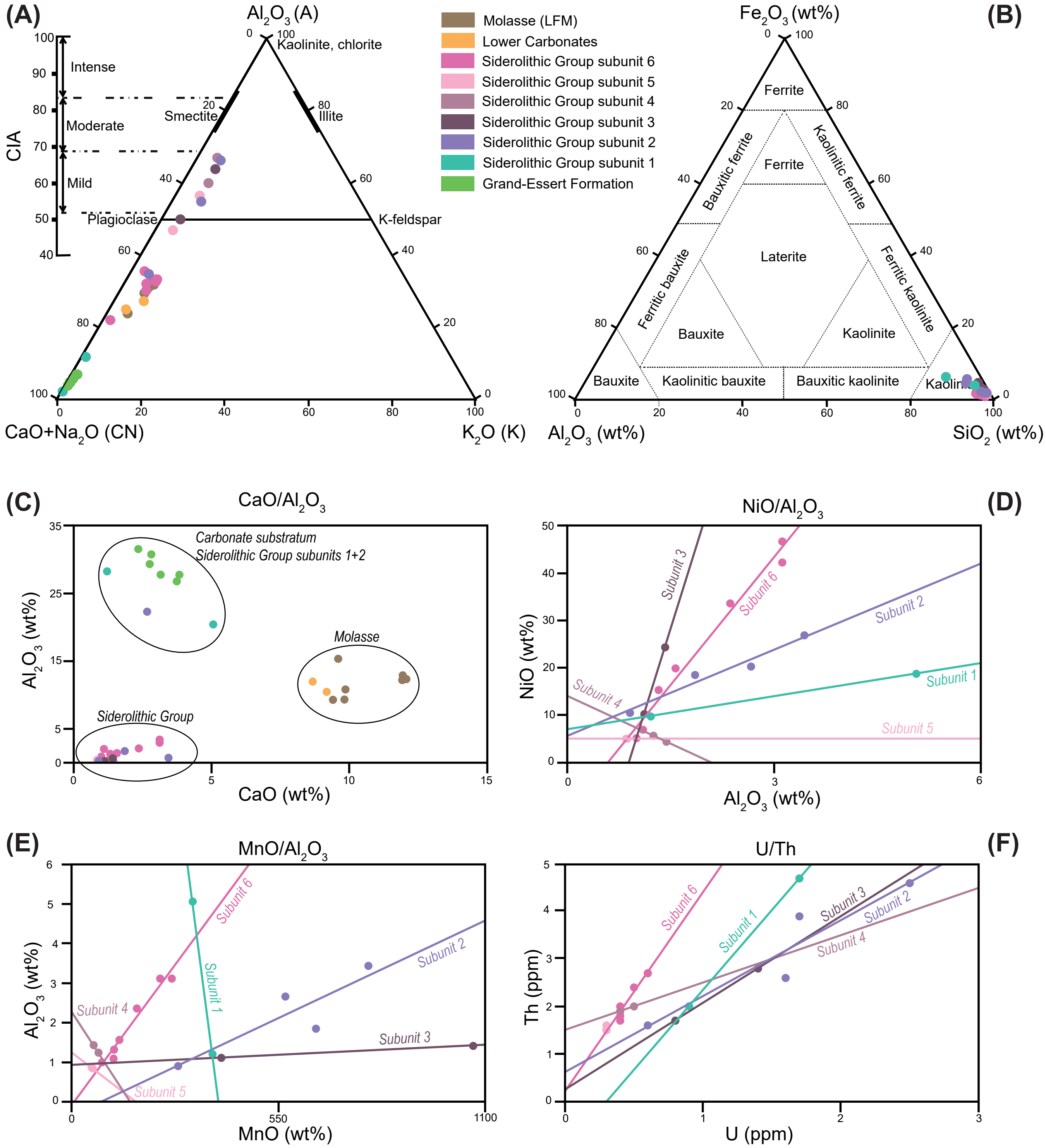

Figure 10 – **(A)** CN-A-K ternary diagram of Al_2O_3–(Ca + Na_2O)–K_2O for the K-Pg samples (Nesbitt & Young, 1982). **(B)** Al_2O_3-SiO_2-Fe_2O_3 ternary plot illustrating mineralogical classification (Schellmann, 1986). Bivariate plots of CaO/Al_2O_3 **(C)**, NiO/Al_2O_3 **(D)**, MnO/Al_2O_3 **(E)**, and U/Th **(F)**.

where karst development and sediment infill varied in response to paleoclimate shifts and fault development (Kelemen et al., 2022).

The geochemical and mineralogical signatures of the Siderolithic Group at GEo-02 highlight the strong climatic influence on epigenic karstification, shaping karst evolution and weathering profiles.

5.2 Depositional processes and lithological variations of the Siderolithic Group

The karst system developed at the top of Cretaceous carbonates, observed in GEo-02, acted as a sediment trap when tectonically associated with subsidence, with subsequence infill of fluvial and aeolian deposits across the identified six subunits, reflecting multiphase processes driven by climate, tectonics and sediment supply (Ellis & Singer, 2007; Radwan, 2020; Van Wagoner et al., 1990). Gamma ray variations (Figure 3) highlight these shifts, marking the transition between major depositional environments within the Siderolithic Group.

5.2.1 Fluvial sequence of the Siderolithic Group (Subunits 1–3)

The lower subunits record fluvially-dominated deposition under the influence of a tropical climate and high detrital input from the exposed highlands indicated by increasing CIA values (2 to 66 %) (Mack et al., 1993; Retallack, 1997). Subunit 1 marks the carbonate-siliciclastic transition, characterised by Fe oxides and kaolinite enrichment, related to prolonged subaerial exposure and pedogenesis (Wright, 2008; Wright & Tucker, 2009). The increasing detrital subangular quartz and kaolinite content and elevating gamma ray signal of subunit 2 (Figure 9) signals intensified weathering (Folk, 1980). Dolomite formation in a continental setting suggests episodic stagnant water conditions and microbial activity in floodplain ponds or abandoned channels (Compton, 1988). Apatite (Figure 5H) is linked to organic-rich conditions and localised phosphogenesis, likely driven by the decay of organic matter in low-energy floodplain settings (Sánchez-Román et al., 2008). The elevated siderite and phosphate concentrations suggest anoxic conditions that promoted iron precipitation and phosphorus retention (Berner, 1981; Singer, 1984). These trends indicate restricted water circulation, organic matter accumulation, and reducing conditions facilitated phosphogenesis (Postma, 1982).

5.2.2 Aeolian sequence (Subunits 4–6)

The 95 m-thick aeolian sequence in borehole GEo-02 (725 to 630 m MD) represents a significant climatic shift from fluvial to aeolian deposition, indicating progressive aridification. The well-sorted, coarse, and highly rounded quartz grains in this clay-poor sandstone, coupled with low gamma ray values and declining CIA values (from 66 to 32 %) (Figure 10A), reflect a mature sedimentary system where such sorting and rounding are more consistent with prolonged aeolian transport and mechanical abrasion than fluvial processes (Kok et al., 2012; Lancaster, 2020; Pye & Tsoar, 2009; Wang et al., 2021).

The onset of aeolian deposition in subunit 4, is marked by moderate gamma ray values (45 API) and intermediate CIA values (59 to 66 %), indicating reworked fluvial sediments mixed with increasing aeolian input. Limited clay, Fe_2O_3 (2.55 wt%), and Mn (46.64 ppm) content suggest fluctuating redox conditions due to episodic moisture availability (Pye & Tsoar, 2009).

The lower gamma ray values, quartz enrichment (> 94 wt%), depleted Mn, Sr, V, Zn, and Al_2O_3 content of subunits 5 and 6 (Figure 8), combined with well-rounded quartz grains, indicate a progressively stronger aeolian signature characterised by high compositional maturity and minimal clay input.

The textural maturity of subunit 5, indicated by well-sorted, matrix-free, rounded quartz grains, reflects prolonged aeolian transport and reworking, consistent with desert sedimentation models (Folk, 1980; Kocurek et al., 1999; Mountney, 2011). The increasing quartz content, along with decreasing CIA and gamma ray values, further confirms the dominance of aeolian processes (Mountney, 2011; Pettijohn et al., 1972).

At the upper boundary of subunit 6, illite-rich siltstone and enrichment in Mn, Ba, K_2O, and Na_2O suggest a lacustrine transition within a closed-basin system, likely influenced by chemical leaching from overlying units (Alonso-Zarza & Tanner, 2006; Gierlowski-Kordesch & Kelts, 1994).

5.3 Diagenetic evolution and reservoir implications

Diagenetic processes in the Siderolithic Group have significantly influenced its mineral composition, porosity evolution, and fluid flow characteristics, shaping its potential as a reservoir unit.

5.3.1 Post-depositional processes—early diagenesis

The siderite, dolomite, apatite, and pyrite paragenesis, along with a high LOI of subunit 1, suggests diagenetic alteration under anoxic conditions. This mineral assemblage reflects microbial degradation of organic matter, which facilitated sulfate reduction and authigenic mineral precipitation (Compton, 1988). Under reducing conditions, the reduction of sulphate (SO_4^{2-} to H_2S) and ferric iron (Fe^{3+} to Fe^{2+}) likely led to pyrite formation, while elevated phosphate (PO_4^{3-}) concentrations favoured apatite precipitation (Berner, 1985; Varadachari et al., 2006). The decomposition of organic matter releases NH_3 and CO_2, leading to increased alkalinity and promoting carbonate precipitation in supersaturated pore waters. This process likely favoured siderite over dolomite as a diagenetic cement in the sandstone matrix, due to the increased Fe^{2+} availability under reducing conditions (Crisogono Vasconcelos (1, 2), 1997; Dejong et al., 2013; Van Lith et al., 2003; Warren, 2000; Warthmann et al., 2000; Zhang et al., 2012).

The high Mn content in subunit 1, closely linked to terra rossa sediments, suggests Fe^{3+} and Mn^{4+} reduction during wet periods, enhancing their mobility and incorporation into diagenetic minerals (Gasparatos, 2012). Similar Fe-Mn remobilisation has been observed in terra rossa formations near Lyon, France (Martini, 1965), where fluctuating redox conditions regulated element mobility and secondary precipitation.

Early siderite cementation likely reduced primary porosity and might have contributed to the sandstone framework stabilisation by resisting compaction. During burial diagenesis, the dissolution of siderite under mesogenetic conditions (> 120 °C) may have contributed to secondary porosity development, with the released Fe^{2+} promoting the precipitation of Fe-oxides and authigenic clay minerals (Vuillemin et al., 2019).

5.3.2 Burial diagenesis and porosity relevance

Burial diagenesis in the Siderolithic Group significantly influenced mineral composition and porosity evolution, with siderite, kaolinite, and chlorite as dominant phases (Figure 9). These diagenetic transformations, driven by fluid interactions and temperature variations, modified reservoir quality by either occluding through carbonate and clay cementation or preserving porosity through selective dissolution and clay coatings (Morad et al., 2010).

The presence of siderite suggests Fe-carbonate precipitation under reducing conditions, facilitated by the dissolution of subaerially exposed carbonates. This process enriched descending fluids in Ca^{2+} and HCO^{3-} ions, leading to the reaction:

$$Fe^{2+}_{(aq)} + HCO_3^{-}{}_{(aq)} \rightleftharpoons FeCO_{3(s)} + H^{+}_{(aq)} \qquad (3)$$

(Curtis, 1985). Petrographic examples from subunit 2 (Figure 5E) and subunit 6 (Figure 7C) confirm the occurrence of siderite cements, which likely reduced primary porosity during early burial. However, partial siderite dissolution in Figure 5E and Figure 7E demonstrates that mesogenetic burial enhanced secondary porosity development in localised domains. These Fe-rich carbonate cements thus record episodic anoxic conditions in the phreatic zone, where Fe^{2+} availability from groundwater circulation was crucial for siderite precipitation.

The formation of chlorite reflects secondary diagenetic processes, likely driven by kaolinite alteration during burial (Iljima & Matsumoto, 1982; Wieland, 1976, 1979). Based on (Hutcheon, 1990), the reaction:

$$2\,Al_2Si_2O_5(OH)_4 + 5\,Fe_2O_3 + 2\,SiO_2 + 4\,H_2O + 2.5\,C \rightleftharpoons Fe_{10}Al_4Si_6O_{20}(OH)_{16} + 2.5\,CO_2 \qquad (4)$$

illustrates how kaolinite, Fe-oxides, and silica can react to form authigenic chlorite. In subunit 4 (Figure 6C) and subunit 6 (Figure 7E), chlorite occurs together with kaolinite and partly replaces siderite, consistent with this reaction. Chlorite coatings also played a crucial role in porosity preservation by preventing quartz overgrowths (Charlaftis et al., 2021; Pittman et al., 1992), a feature documented in Figure 6C and E.

Additionally, siderite destabilisation during mesogenetic diagenesis (> 120 °C) may have provided an Fe source for chlorite precipitation (Curtis, 1985), according to the reaction:

$$5\,FeCO_3 + SiO_2 + Al_2Si_2O_5(OH)_4 \rightleftharpoons Fe_5Al_2Si_3O_{10}(OH)8 + 5\,CO_2 \qquad (5)$$

The siderite-chlorite-kaolinite associations visible in Figures 5C and E, 7C, 6B, C, E and F support this interpretation. Furthermore, the co-occurrence of chlorite and fine quartz grains (Figure 6E) may indicate localised quartz dissolution, enhancing secondary porosity.

5.4 Provenance of the Siderolithic Group

The provenance of sediments in the Siderolithic Group was controlled by regional paleotectonic and paleoclimatic processes, which dictated sediment routing, depositional environments, and lithological evolution.

5.4.1 Aeolian and fluvial sources

The provenance of the Siderolithic Group reflects the interplay between tectonic uplift and subsidence, sediment transport, and climatic variability, resulting in a mixed aeolian and fluvial signature. The occurrence of millimetre-scale, well-rounded quartz grains record prolonged aeolian abrasion, whereas fine, subangular grains indicate shorter fluvial transport with limited reworking (Figure 11). These contrasting grain populations highlight the dual influence of aeolian and fluvial processes in the depositional system.

Quartz grains within the Siderolithic Group were sourced from both primary and recycled sources, reflecting regional tectonic evolution. Primary sources likely included Triassic sandstones from the French Massif Central, the Vosges and Black Forest, during the ECRIS (Pfiffner, 2014). Secondary sources included the reworking of pre-Eocene sandstone formations, such as the Perte-du-Rhône Formation (Pictet et al., 2016), and detrital quartz from dissolution of Cretaceous carbonates.

Initially, subangular to angular quartz grains were transported and redeposited in high-energy fluvial systems (Tucker & Wright, 2009). As conditions shifted towards increasing aridity, these primary and recycled sources were subjected to prolonged aeolian reworking, leading to the progressive abrasion and rounding of quartz grains by wind-driven transport (Kok et al., 2012; Wang et al., 2021). The variation in grain shape and sorting indicates an initial fluvial deposition, later modified by aeolian processes. This transition from fluvially reworked sediments to well-sorted, mature aeolian deposits is evident in the stratigraphic profile of the Siderolithic Group subunits in the Geo-02 well.

5.4.2 Tectonic framework of the Siderolithic Group sedimentation

The Eocene paleogeographic configuration of the Geneva Basin, between the Bresse Graben to the west and the Alpine Tethys Ocean to the south (Pfiffner, 2014), strongly influences depositional conditions. Together, sediment supply from the Bresse Graben and episodic marine incursions from the Alpine Tethys Ocean created supratidal environments where aeolian and fluvial processes overlapped (Liu & Coulthard, 2015; Zular et al., 2018) (Figure 12).

A potential local sandstone analogue, the Rochers de Faverges near Salève (Joukowsky & Favre, 1913; Sesiano, 2017), exhibits large-scale cross-bedding typical of aeolian dune deposits, a feature that might be comparable to the Siderolithic Group, suggesting a similar sedimentary evolution. Ongoing detrital U–Pb zircon analysis will provide a direct comparison between this formation and the Siderolithic Group at Geo-02, refining provenance interpretations and source-to-sink dynamics within the Geneva Basin.

5.4.3 Geochemical stratigraphy and provenance indicators of the Siderolithic Group related to shifting climate conditions

Geochemical proxies are valuable tools for refining the stratigraphy of the Siderolithic Group, as they capture lithological differences between sub-units driven by changes in depositional environments, source areas and climate-induced weathering. The CIA (Figure 10A) is higher in subunits 2, 3, and 4, indicating less mature, matrix-rich fluvial deposits, while subunits 5 and 6 have lower CIA values, reflecting highly mature, quartz-dominated aeolian sediments (Nesbitt & Young, 1982; Retallack, 1997).

The MnO/Al_2O_3 and U/Th ratios (Figure 10E and F) highlight two geochemical clusters, with subunits 1–3 showing similar signatures, consistent with fluvial deposits influenced by pedogenic weathering, and subunits 4–6 forming a distinct group, indicating aeolian reworking and increasing sediment maturity (Bosboom, Abels, et al., 2014; Methner et al., 2016).

The NiO/Al_2O_3 ratio (Figure 10D) differentiates subunits 1 and 2, which are Al_2O_3-enriched due to intense weathering, from subunit 6, which has the highest NiO values, likely reflecting input from the overlying Molasse (Dequincey et al., 2005). The CaO/Al_2O_3 ratio

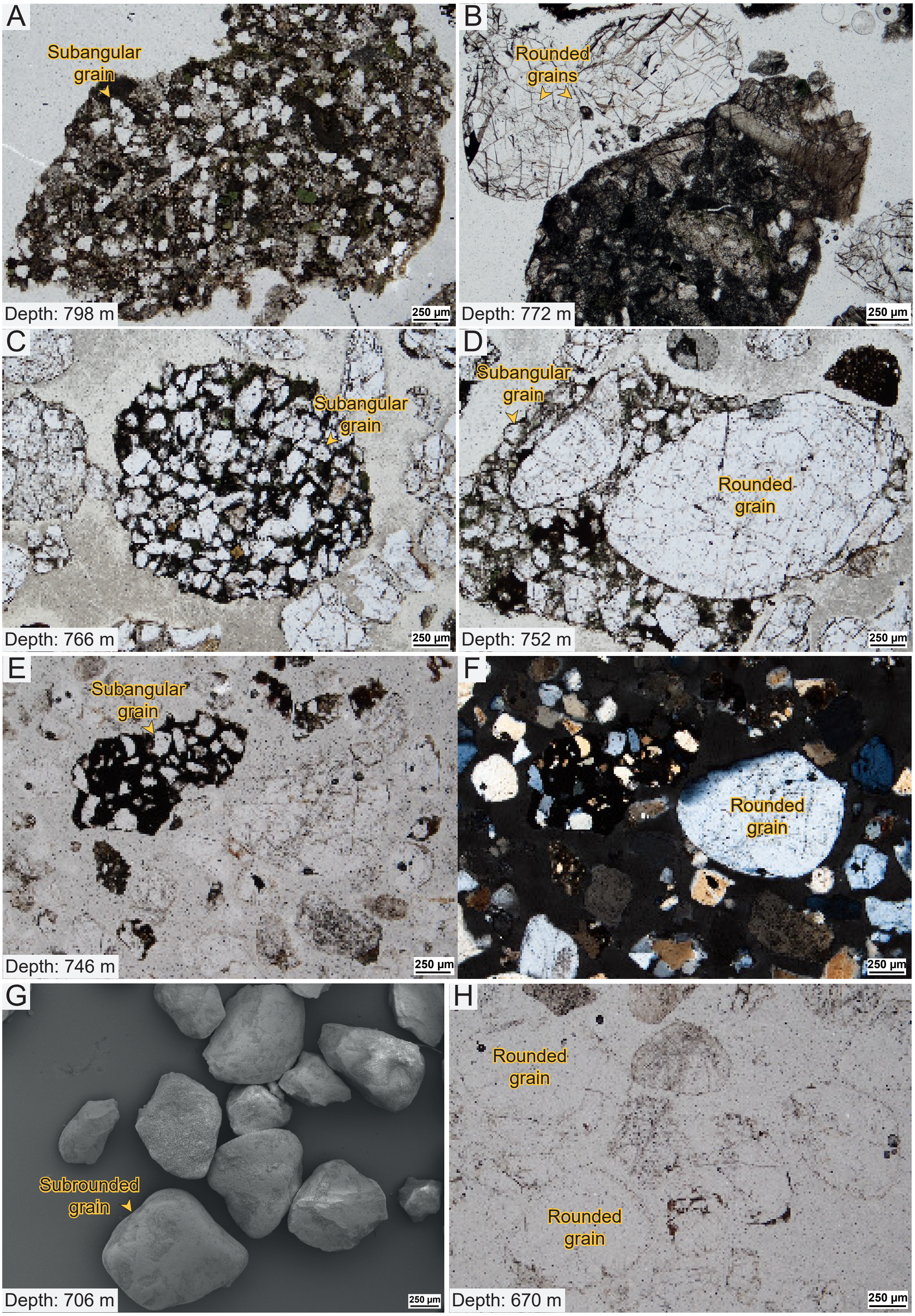

Figure 11 – Optical microscopy images of the GEo-02 well thin sections (**A**, **B**, **C**, **D**, **E** and **H**; plane polarized, **F**; cross-polarized, **G**; SEM image). **(A)**, **(C)** and **(E)** Fine sandstone with subangular quartz grains. **(B)**, **(F)**, **(G)** and **(H)** Coarse to very coarse sandstone with rounded quartz grains. **(D)** Sandstone with a bimodal distribution of fine subangular quartz grains with coarse to very coarse rounded quartz grains.

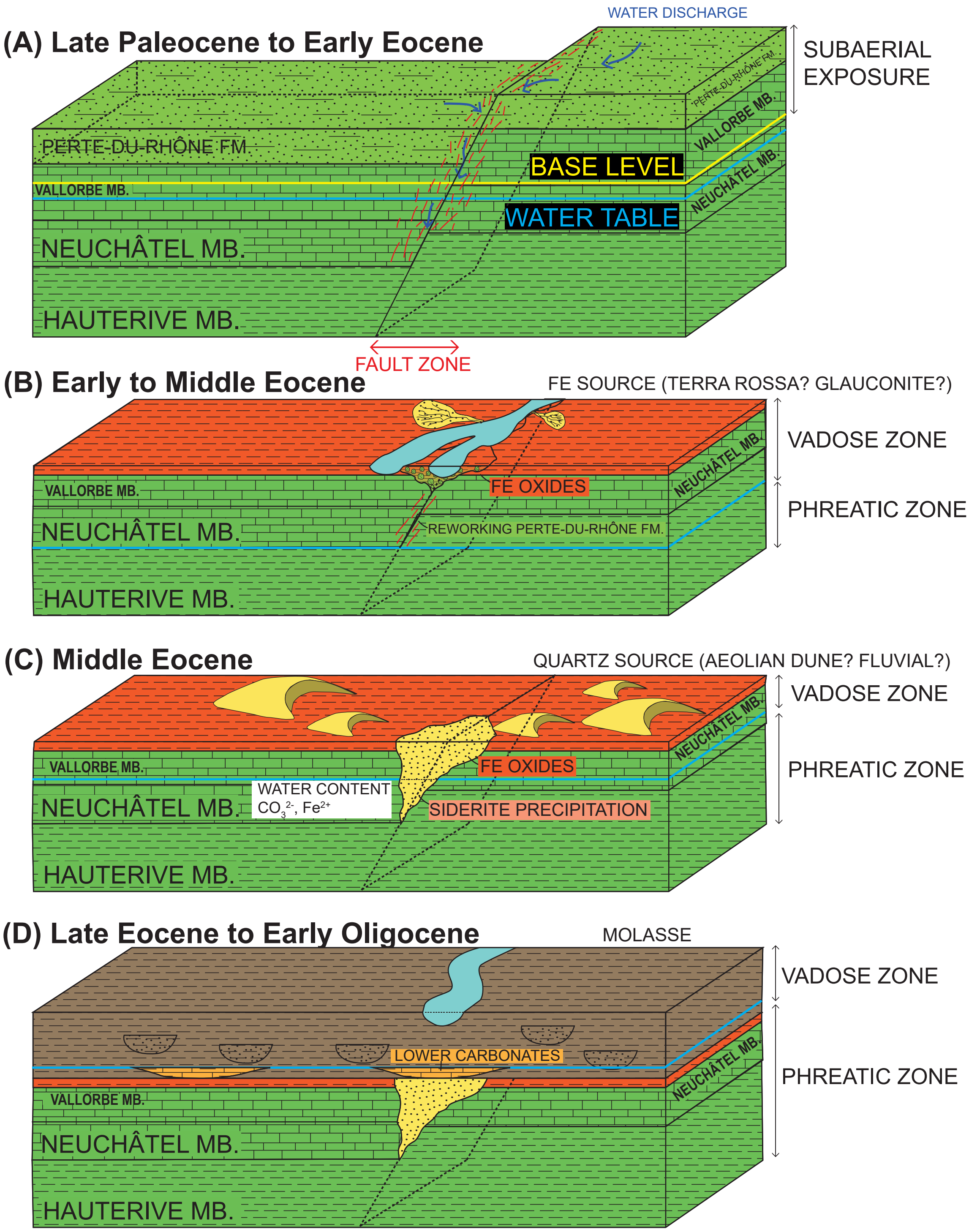

Figure 12 – Depositional and structural model of the Cretaceous–Paleogene (K–Pg) evolution. **(A)** Late Paleocene to Early Eocene: Subaerial exposure with base level controlled by relative sea level, which governed erosion and accommodation. The water table marks the boundary between the vadose (unsaturated) and phreatic (saturated) zones. Sediment input came from the Perte-du-Rhône Formation. The Vallorbe Member is illustrated above the Neuchâtel Member for conceptual clarity, although these units do not directly or uniformly overlie one another stratigraphically. **(B)** Early to Middle Eocene: Under warm and humid climatic conditions, terra rossa developed on the carbonate substratum. This weathering product, together with glauconite released from dissolution of the Perte-du-Rhône Formation, likely supplied Fe to the system. **(C)** Middle Eocene: Yellow features represent conceptual epikarst conduits formed along fault zones and enlarged by meteoric water dissolution under humid conditions. These dissolution pathways acted as channels for quartz-rich sediment of aeolian or fluvial origin. Siderite precipitation took place in the phreatic zone where Fe^{2+}, CO_2, and groundwater circulation intersected. **(D)** Late Eocene to Early Oligocene: Deposition of the Molasse overlies the karstified system. Continued subsidence and compaction of the infill may have created accommodation space for lacustrine carbonates, which accumulated in localised depressions within the basin.

(Figure 10C) delineates the Cretaceous-Paleogene boundary, distinguishing the Siderolithic Group from the underlying Cretaceous substratum and the overlying LFM, underlining the shift from carbonate-dominated to siliciclastic-rich environments.

These geochemical trends confirm a progressive transition from fluvial to aeolian deposition, where early fluvial sediments (subunits 1–3) were intensely weathered, while later aeolian deposits (subunits 4–6) became more compositionally mature through prolonged reworking and sorting. This evolution reflects climate-driven shifts from humid conditions favouring chemical weathering and fluvial transport to arid environments promoting mechanical sediment reworking.

5.4.4 Volcanic input during the Middle Eocene Climatic Optimum (MECO)

Geochemical signatures indicate an indirect volcanogenic contribution to sedimentation in the terrestrial Siderolithic Group, particularly in subunits 1, 2, and 3, where elevated Mn concentrations (Figure 8B) and elemental ratios such as MnO/Al_2O_3, NiO/Al_2O_3 (Figure 10D), and U/Th (Figure 10F) reflect input of pyroclastic material enriched in Fe and Mn (Maghfouri et al., 2017). These elements, commonly associated in volcanic ash, have been mobilised during oxidative weathering and concentrated through pedogenic processes under fluctuating redox conditions (Öztürk et al., 2002) with possible sources including reworked basaltic ash or bauxitic soils formed during the PETM (c. 56 Ma) (Wilkinson et al., 2017), andesitic volcanism related to Neotethys subduction (c. 35 Ma) (van der Boon et al., 2021), and erosion of Upper Cretaceous Mn-rich nodules from the Narlay Formation (Strasser et al., 2016).

The high Hg content in subunits 3 and 4 (Figure 8B) supports a volcanic origin (Sial et al., 2013) and may reflect enhanced volcanic activity during major global warming events such as the PETM and the MECO, both characterised by with increased volcanic emissions, rainfall, and intensified weathering (Bosboom, Abels, et al., 2014; Sial et al., 2013; Tremblin et al., 2022). MECO likely enhanced sediment recycling through intensified erosion in the hinterland, and introducing volcanogenic aerosols into terrestrial deposits.

The Hg enrichment in the Bartonian Siderolithic Group may reflect a continental record of the MECO, dated between 40.5 and 40.0 Ma (Bosboom, Dupont-Nivet, et al., 2014; Methner et al., 2016; Mulch et al., 2015; Peris Cabré et al., 2023; Sharma et al., 2024) Given its link to increased volcanic outgassing and greenhouse conditions (van der Boon et al., 2021), the Siderolithic Group geochemistry reflects both direct volcanic input and intensified chemical weathering under fluctuating climatic conditions (Sial et al., 2013; van der Boon et al., 2021).

6 Conclusions

This study provides a detailed sedimentological, mineralogical, geochemical, and stratigraphical characterisation of the Siderolithic Group within the Geneva Basin using high-resolution data from the GEo-02 geothermal exploration well. The exceptional 158 m thickness of the Siderolithic Group, deposited within a tectonically controlled depression developed in karstified Lower Cretaceous carbonates, challenges previous subsurface interpretations and highlights the importance of integrating borehole data with seismic and outcrop analogues.

Six stratigraphic subunits were identified, recording a transition from fluvial to dominantly aeolian deposition. The lower subunits, characterised by high LOI, terra rossa profiles, and kaolinite-rich clay assemblages, indicate intense chemical weathering under humid conditions during the MECO. The upper subunits, in contrast, consist of well-sorted, quartz-rich sandstones with low clay content and gamma ray values, reflecting increasing aridity and sediment maturity.

The Siderolithic infill exhibits variable gamma ray responses and a heterogeneous distribution of quartz grain textures, supporting a multi-phase sedimentation history involving both fluvial and aeolian processes. This complex infill geometry is closely linked to tectonic structures, particularly a NE–SW fault system associated with the ECRIS, which created localised subsidence zones and sediment traps.

The observed mineralogical and geochemical signatures suggest potential sediment sources from eroded crystalline basement, fluvial systems, aeolian dunes, and reworked coastal deposits. These pathways were likely influenced by regional tectonics, including the evolution of the Bresse Graben and the proximity to the Alpine Tethys margin. These interpretations will be further tested through ongoing provenance analysis using detrital zircon dating, which is expected to clarify sediment sources and transport dynamics.

Diagenetic features, including early siderite cementation followed by burial alteration to chlorite, significantly influenced porosity evolution in the Siderolithic Group. Siderite cement locally reduced pore space, but its partial dissolution likely generated secondary porosity. Additionally, chlorite coatings may have inhibited quartz overgrowths, contributing to pathways for fluid flow.

Geochemical signatures—including elevated mercury concentrations and REE patterns—suggest a volcanic influence during deposition, likely tied to the Neotethys subduction under the warm-humid conditions of the MECO. This geochemical imprint, combined with Bartonian-age correlations and paleosol development, positions the Siderolithic Group in GEo-02 as one of the few well-preserved continental records of the MECO in Western Europe.

This study reconstructs the complex depositional, diagenetic, and tectonic evolution of the Siderolithic Group and highlights its significance as both a paleoclimate archive and a potential geothermal reservoir in the Western Alpine Foreland Basin.

Acknowledgements

This work was carried out in the framework of the ongoing geothermal exploration program known as GEothermies promoted by the SIG (Services Industriels de Genève) and the Canton of Geneva. The authors would like to thank Michel Meyer, Carole Nawratil de Bono and Jérôme Caudroit at SIG for providing access to the cuttings and digital logs of the GEo-02 borehole. The authors are thankful to Dr Davide Carraro and Prof. Nina Zeyen (University of Geneva) for performing X-ray clay fraction diffraction analyses, and Dr Antoine De Haller (University of Geneva) for QEMSCAN and XRF analyses and technical support with the ioGAS software.

Data and code availability

All the data are provided in the supplementary materials attached to this paper. Supplementary data to this article can be found with the online version of this article.

Supplementary material

Supplementary data to this article is available online at doi:10.57035/journals/sdk.2026.e41.1914.

Conflict of interest statement

The authors declare that they have no known competing financial interests or personal relationships that could have appeared to influence the work reported in this paper.

Artificial intelligence use statement

Generative AI tools were used for language polishing only; all scientific content and conclusions were produced by the authors.

Funding

This research was funded by the Services Industriels de Genève (SIG).

Citing this Research Article

To cite this paper use the following information:

Authors
Aurélia Crinière, Yasin Makhloufi, Ovie Emmanuel Eruteya, Andrea Moscariello

Title
Origin and composition of the Siderolithic Group, Geneva Basin (GEo-02 well)

Short Title
The Siderolithic Group, Geneva Basin (GEo-02 well)

Publishing Information
Publication: Sedimentologika
Volume: 4
Issue: 1
Year: 2026
DOI: 10.57035/journals/sdk.2026.e41.1914
Language: en
License: CC-BY 4.0

References

Agosta, F., Alessandroni, M., Antonellini, M., Tondi, E., & Giorgioni, M. (2010). From fractures to flow: A field-based quantitative analysis of an outcropping carbonate reservoir. *Tectonophysics*, *490*(3–4), 197–213. https://doi.org/10.1016/j.tecto.2010.05.005

Allen, P. A., Crampton, S. L., & Sinclair, H. D. (1991). The inception and early evolution of the North Alpine Foreland Basin, Switzerland. *Basin Research*, *3*(3), 143–163. https://doi.org/10.1111/j.1365-2117.1991.tb00124.x

Alonso-Zarza, A. M., & Tanner, L. H. (Eds.). (2006). *Paleoenvironmental Record and Applications of Calcretes and Palustrine Carbonates*. Geological Society of America. https://doi.org/10.1130/spe416

Banfield, J. F., & Eggleton, R. A. (1990). Analytical Transmission Electron Microscope Studies of Plagioclase, Muscovite, and K-Feldspar Weathering. *Clays and Clay Minerals*, *38*(1), 77–89. https://doi.org/10.1346/ccmn.1990.0380111

Bárdossy, György. (1982). *Karst bauxites: Vol. 14: Developments in Economic Geology*. Elsevier.

Bautista, F., Palacio-Aponte, G., Quintana, P., & Zinck, J. A. (2011). Spatial distribution and development of soils in tropical karst areas from the Peninsula of Yucatan, Mexico. *Geomorphology*, *135*(3–4), 308–321. https://doi.org/10.1016/j.geomorph.2011.02.014

Beck, C., Deville, E., Blanc, E., Philippe, Y., & Tardy, M. (1998). Horizontal shortening control of Middle Miocene marine siliciclastic accumulation (Upper Marine Molasse) in the southern termination of the Savoy Molasse Basin (northwestern Alps/southern Jura). In A. Mascle, C. Puigdefàbregas, H. P. Luterbacher, & Manuel Fernàndez (Eds.), *Cenozoic Foreland Basins of Western Europe: Vol. 134: Special Publications* (pp. 263–278). Geological Society of London. https://doi.org/10.1144/gsl.sp.1998.134.01.12

Becker, D. (2003). *Paléoécologie et paléoclimats de la Molasse du Jura (Oligo-Miocène): apport des Rhinocerotoidea (Mammalia) et des minéraux argileux* [Doctoral thesis, Université de Fribourg]. FOLIA - Fribourg Open Library and Archive. https://doi.org/10.51363/unifr.sth.2025.021

Berger, J.-P., Reichenbacher, B., Becker, D., Grimm, M., Grimm, K., Picot, L., Storni, A., Pirkenseer, C., & Schaefer, A. (2005). Eocene-Pliocene time scale and stratigraphy of the Upper Rhine Graben (URG) and the Swiss Molasse Basin (SMB). *International Journal of Earth Sciences*, *94*(4), 711–731. https://doi.org/10.1007/s00531-005-0479-y

Berner, R. A. (1981). A New Geochemical Classification of Sedimentary Environments. *Journal of Sedimentary Research*, *Vol. 51*(2), 359–365. https://doi.org/10.1306/212F7C7F-2B24-11D7-8648000102C1865D

Berner, R. A. (1985). Sulphate reduction, organic matter decomposition and pyrite formation. *Philosophical Transactions of the Royal Society of London. Series A, Mathematical and Physical Sciences*, *315*(1531), 25–38. https://doi.org/10.1098/rsta.1985.0027

Blondel, T. (1988). La montagne du Vuache (Jura méridional): un exemple de structure géologique d'apparence simple mais de formation complexe. *Le Globe. Revue genevoise de géographie*, *128*(1), 16–38. https://doi.org/10.3406/globe.1988.1252

Boero, V., & Schwertmann, U. (1989). Iron oxide mineralogy of terra rossa and its genetic implications. *Geoderma*, *44*(4), 319–327. https://doi.org/10.1016/0016-7061(89)90039-6

Bohaty, S. M., & Zachos, J. C. (2003). Significant Southern Ocean warming event in the late middle Eocene. *Geology*, *31*(11), 1017. https://doi.org/10.1130/G19800.1

Bohaty, S. M., Zachos, J. C., Florindo, F., & Delaney, M. L. (2009). Coupled greenhouse warming and deep-sea acidification in the middle Eocene. *Paleoceanography*, *24*(2). https://doi.org/10.1029/2008pa001676

Bohnsack, D., Potten, M., Pfrang, D., Wolpert, P., & Zosseder, K. (2020). Porosity–permeability relationship derived from Upper Jurassic carbonate rock cores to assess the regional hydraulic matrix properties of the Malm reservoir in the South German Molasse Basin. *Geothermal Energy*, *8*(1). https://doi.org/10.1186/s40517-020-00166-9

Bosboom, R. E., Abels, H. A., Hoorn, C., van den Berg, B. C. J., Guo, Z., & Dupont-Nivet, G. (2014). Aridification in continental Asia after the Middle Eocene Climatic Optimum (MECO). *Earth and Planetary Science Letters*, *389*, 34–42. https://doi.org/10.1016/j.epsl.2013.12.014

Bosboom, R. E., Dupont-Nivet, G., Grothe, A., Brinkhuis, H., Villa, G., Mandic, O., Stoica, M., Huang, W., Yang, W., Guo, Z., & Krijgsman, W. (2014). Linking Tarim Basin sea retreat (west China) and Asian aridification in the late Eocene. *Basin Research*, *26*(5), 621–640. https://doi.org/10.1111/bre.12054

Boscolo Galazzo, F., Thomas, E., Pagani, M., Warren, C., Luciani, V., & Giusberti, L. (2014). The middle Eocene climatic optimum (MECO): A multiproxy record of paleoceanographic changes in the southeast Atlantic (ODP Site 1263, Walvis Ridge). *Paleoceanography*, *29*(12), 1143–1161. https://doi.org/10.1002/2014pa002670

Bragg, W. H. (1913). The reflection of X-rays by crystals. *Proceedings of the Royal Society of London. Series A, Containing Papers of a Mathematical and Physical Character*, *88*(605), 428–438. https://doi.org/10.1098/rspa.1913.0040

BRGM. (2003). *Carte géologique de la France à 1/1 000 000* (6th ed.) [Geologic map]. Bureau de Recherches Géologiques et Minières.

Charlaftis, D., Jones, S. J., Dobson, K. J., Crouch, J., & Acikalin, S. (2021). Experimental study of chlorite authigenesis and influence on porosity maintenance in sandstones. *Journal of Sedimentary Research*, *91*(2), 197–212. https://doi.org/10.2110/jsr.2020.122

Charollais, J.-J., Busnardo, R., Cardin, M., Clavel, B., Decrouez, D., Delamette, M., Gorin, G., Lepiller, M., Mondain, P.-H., Rosset, J., & Villars, F. (1988). *Notice explicative, Carte géol. France (1/50 000), feuille Annecy-Bonneville (678)* [Explanatory notes]. Bureau Des Recherches Géologiques et Minières. http://ficheinfoterre.brgm.fr/Notices/0678N.pdf

Charollais, J.-J., Clavel, B., Schroeder, R., Busnardo, R., & Horisberger, P. (1994). Mise en évidence de l'émersion post-urgonienne et de la lacune du Barrémien-Bédoulien inférieur/moyen dans le Jura neuchâtelois. In *Calcaires urgoniens et grès verts jurassiens et delphino-helvétiques* (pp. 57–79). Université de Genève, Département de géologie et paléontologie; Archive ouverte UNIGE. https://archive-ouverte.unige.ch/unige:120352

Charollais, J.-J., Mastrangelo, B., Strasser, A., Piuz, A., Granier, B., Monteil, E., Ruchat, C., & Savoy, L. (2023). Lithostratigraphie, biostratigraphie, cartographie et géologie structurale du Mont Salève, entre l'Arve et les Usses (Haute Savoie, France). *Revue De Paléobiologie*, *42*(1), 1–127. https://doi.org/10.5281/zenodo.7446048

Charollais, J.-J., Plancherel, R., Monjuvent, G., & Debelmas, J. (1998). *Notice explicative, Carte géol. France (1/50 000), feuille Annemasse (654)* [Explanatory notes]. Bureau Des Recherches Géologiques et Minières. http://ficheinfoterre.brgm.fr/Notices/0654N.pdf

Charollais, J.-J., Weidmann, M., Berger, J.-P., Engesser, B., Hotellier, J.-F., Gorin, G., Reichenbacher, B., & Schäfer, P. (2007). La Molasse du bassin franco-genevois et son substratum. *Archives Des Sciences*, *60*(2–3), 59–174. https://doi.org/10.5169/seals-738416

Charollais, J.-J., & Wellhauser, F. (1962). Contribution à l'étude des Marnes à foraminifères des chaînes subalpines (Hte-Savoie, France). *Bulletin Der Vereinigung Schweizerischer Petroleumgeologen Und Petroleumingenieure*, *29*(76), 21–38. https://doi.org/10.5169/seals-192061

Charollais, J.-J., Wernli, R., Mastrangelo, B., Metzger, J., Busnardo, R., Clavel, B., Conrad, M., Davaud, E., Granier, B., Saint Martin, M., & Weidmann, M. (2013). Présentation d'une nouvelle carte géologique du Vuache et du Mont de Musièges (Haute-Savoie, France): stratigraphie et tectonique. *Archives Des Sciences*, *66*, 1–64. https://doi.org/10.5169/seals-738474

Chelle-Michou, C., Do Couto, D., Moscariello, A., Renard, P., & Rusillon, E. (2017). Geothermal state of the deep Western Alpine Molasse Basin, France-Switzerland. *Geothermics*, *67*, 48–65. https://doi.org/10.1016/j.geothermics.2017.01.004

Chevalier, G., Diamond, L. W., & Leu, W. (2010). Potential for deep geological sequestration of CO2 in Switzerland: a first appraisal. *Swiss Journal of Geosciences*, *103*(3), 427–455. https://doi.org/10.1007/s00015-010-0030-4

Činčura, J. (1990). Characteristic features of paleoalpine and epipaleoalpine landmass of the West Carpathians. *Geologica Carpathica*, *41*, 29–38.

Clerc, N., & Moscariello, A. (2020). A revised structural framework for the Geneva Basin and the neighbouring France region as revealed from 2D seismic data : implications for geothermal exploration. *Swiss Bulletin Für Angewandte Geologie*, *25*(1–2), 109–131. https://doi.org/10.5169/seals-977312

Collet, L. W., & Paréjas, E. (1936a). Contribution à l'étude du Tertiaire du Salève. N° 2, La région comprise entre les Essert et les Usses. *Compte Rendu Des Séances De La Société De Physique Et D'histoire Naturelle De Genève*, *53*(2), 95–98. https://doi.org/10.5169/SEALS-743102

Collet, L. W., & Paréjas, E. (1936b). Contribution à l'étude du Tertiaire du Salève. N° 3, Vue d'ensemble. *Compte Rendu Des Séances De La Société De Physique Et D'histoire Naturelle De Genève*, *53*(2), 98–101. https://doi.org/10.5169/seals-743103

Compton, J. S. (1988). Sediment Composition and Precipitation of Dolomite and Pyrite in the Neogene Monterey and Sisquoc Formations Santa Maria Basin Area California. In *Sedimenlology and geochemistry of dolostones: Vol. 43: SEPM Special Publication* (pp. 53–64). SEPM Society for Sedimentary Geology. https://doi.org/10.2110/pec.88.43.0053

Conrad, M. A., & Ducloz, C. (1977). Nouvelle observations sur l'urgonien et le sidérolithique du salève. *Eclogae Geologicae Helvetiae*, *70*(1), 127–141.

Cramwinckel, M. J., Huber, M., Kocken, I. J., Agnini, C., Bijl, P. K., Bohaty, S. M., Frieling, J., Goldner, A., Hilgen, F. J., Kip, E. L., Peterse, F., van der Ploeg, R., Röhl, U., Schouten, S., & Sluijs, A. (2018). Synchronous tropical and polar temperature evolution in the Eocene. *Nature*, *559*(7714), 382–386. https://doi.org/10.1038/s41586-018-0272-2

Crisogono Vasconcelos (1, 2), Judith. (1997). Microbial Mediation of Modern Dolomite Precipitation and Diagenesis Under Anoxic Conditions (Lagoa Vermelha, Rio de Janeiro, Brazil). *SEPM Journal of Sedimentary Research*, *Vol. 67*(3), 378–390. https://doi.org/10.1306/d4268577-2b26-11d7-8648000102c1865d

Crozet, R. (1932). Sidérolithique et latérite. *Annales de Géographie*, *41*(234), 659–660. https://doi.org/10.3406/geo.1932.10712

Curtis, C. D. (1985). Clay mineral precipitation and transformation during burial diagenesis. *Philosophical Transactions of the Royal Society of London. Series A, Mathematical and Physical Sciences*, *315*(1531), 91–105. https://doi.org/10.1098/rsta.1985.0031

D'Onofrio, R., Zaky, A. S., Frontalini, F., Luciani, V., Catanzariti, R., Francescangeli, F., Giorgioni, M., Coccioni, R., Özcan, E., & Jovane, L. (2021). Impact of the Middle Eocene Climatic Optimum (MECO) on Foraminiferal and Calcareous Nannofossil Assemblages in the Neo-Tethyan Baskil Section (Eastern Turkey): Paleoenvironmental and Paleoclimatic Reconstructions. *Applied Sciences*, *11*(23), 11339. https://doi.org/10.3390/app112311339

Daniou, P. (1979). Sur quelques indurations siliceuses présentes dans les faciès dits "Sidérolithiques" des confins de la Charente et du Périgord. *Travaux du Laboratoire de Géographie Physique Appliquée*, *3*(1), 17–44. https://doi.org/10.3406/tlgpa.1979.879

Daniou, P. (1981). Le "sidérolithique" des pays du nord de l'aquitaine : essai de bibliographie critique. *Travaux du Laboratoire de Géographie Physique Appliquée*, *5*(1), 1–74. https://doi.org/10.3406/tlgpa.1981.883

De la Harpe, Ph. (1854). De la formation sidérolitique dans les Alpes. *Bulletin de La Société Vaudoise Des Sciences Naturelles*, *35*, 232–236.

Debelmas, J., Michel, R., & Millot, G. (1961). Silicifications par altération climatique dans les séries alpines. *Travaux Du Laboratoire De Géologie De La Faculté Des Sciences De Grenoble*, *37*, 7–14.

Dejong, J. T., Soga, K., Kavazanjian, E., Burns, S., Van Paassen, L. A., Al Qabany, A., Aydilek, A., Bang, S. S., Burbank, M., Caslake, L. F., Chen, C. Y., Cheng, X., Chu, J., Ciurli, S., Esnault-Filet, A., Fauriel, S., Hamdan, N., Hata, T., Inagaki, Y., ... Weaver, T. (2013). Biogeochemical processes and geotechnical applications: progress, opportunities and challenges. *Géotechnique*, *63*(4), 287–301. https://doi.org/10.1680/geot.sip13.p.017

Delaunay, A. (1984). Contribution à l'interprétation et au reboisement des faciès du Sidérolithique. Le Sidérolithique silicifié. *Revue Forestière Française*, *36*(5), 375. https://doi.org/10.4267/2042/21749

Dequincey, O., Chabaux, F., Leprun, J. -C., Paquet, H., Clauer, N., & Larque, P. (2005). Lanthanide and trace element mobilization in a lateritic toposequence: inferences from the Kaya laterite in Burkina Faso. *European Journal of Soil Science*, *57*(6), 816–830. https://doi.org/10.1111/j.1365-2389.2005.00773.x

Deschamps, M. (1958). Analogie entre les grès et arkoses de la Brenne (Indre) et ceux de Cosne (Aallier). *Académie Des Sciences*, *247*(23), 2167–2170.

Dèzes, P., Schmid, S. M., & Ziegler, P. A. (2004). Evolution of the European Cenozoic Rift System: interaction of the Alpine and Pyrenean orogens with their foreland lithosphere. *Tectonophysics*, *389*(1–2), 1–33. https://doi.org/10.1016/j.tecto.2004.06.011

Durn, G. (2003). Terra Rossa in the Mediterranean region: Parent materials, composition and origin. *Geologia Croatica*, *56*(1), 83–100. https://doi.org/10.4154/gc.2003.06

Durn, G., Ottner, F., & Slovenec, D. (1999). Mineralogical and geochemical indicators of the polygenetic nature of terra rossa in Istria, Croatia. *Geoderma*, *91*(1–2), 125–150. https://doi.org/10.1016/s0016-7061(98)00130-x

Durn, G., Perković, I., Stummeyer, J., Ottner, F., & Mileusnić, M. (2021). Differences in the behaviour of trace and rare-earth elements in oxidizing and reducing soil environments: Case study of Terra Rossa soils and Cretaceous palaeosols from the Istrian peninsula, Croatia. *Chemosphere*, *283*, 131286. https://doi.org/10.1016/j.chemosphere.2021.131286

El-Fawal, F. M., El-Asmar, H. M., & Sarhan, M. A. E.-F. (2011). Depositional evolution of the Middle-Upper Eocene rocks, Fayum area, Egypt. *Arabian Journal of Geosciences*, *6*(3), 749–760. https://doi.org/10.1007/s12517-011-0386-4

Ellis, D. V., & Singer, J. M. (Eds.). (2007). *Well Logging for Earth Scientists* (2nd ed.). Springer. https://doi.org/10.1007/978-1-4020-4602-5

Eruteya, O. E., Crinière, A., & Moscariello, A. (2024). Seismic expression of paleokarst morphologies and associated Siderolithic infill in the Geneva Basin, Switzerland: Implications for geothermal exploration. *Geothermics*, *117*, 102868. https://doi.org/10.1016/j.geothermics.2023.102868

Fernández-Caliani, J. C., Galán, E., Aparicio, P., Miras, A., & Márquez, M. G. (2010). Origin and geochemical evolution of the Nuevo Montecastelo kaolin deposit (Galicia, NW Spain). *Applied Clay Science*, *49*(3), 91–97. https://doi.org/10.1016/j.clay.2010.06.006

Folk, R. L. (1980). *Petrology of Sedimentary Rocks*. Hemphill Publishing Company. http://hdl.handle.net/2152/22930

Gasparatos, D. (2012). Fe-Mn Concretions and Nodules to Sequester Heavy Metals in Soils. In E. Lichtfouse, J. Schwarzbauer, & D. Robert (Eds.), *Environmental Chemistry for a Sustainable World: Vol. 2: Remediation of Air and Water Pollution* (1st ed., pp. 443–474). Springer. https://doi.org/10.1007/978-94-007-2439-6_11

Gierlowski-Kordesch, E., & Kelts, K. (Eds.). (1994). *Global Geological Record of Lake Basins* (Vol. 1). Cambridge University Press.

Goldscheider, N., Mádl-Szőnyi, J., Erőss, A., & Schill, E. (2010). Review: Thermal water resources in carbonate rock aquifers. *Hydrogeology Journal*, *18*(6), 1303–1318. https://doi.org/10.1007/s10040-010-0611-3

Greenwood, D. R., & Wing, S. L. (1995). Eocene continental climates and latitudinal temperature gradients. *Geology*, *23*(11), 1044. https://doi.org/10.1130/0091-7613(1995)023<1044:ECCALT>2.3.CO;2

Guendon, J.-L. (1984). Les paléokarsts des Alpes occidentales du Trias à l'Éocène. *Karstologia : revue de karstologie et de spéléologie physique*, *4*(1), 2–10. https://doi.org/10.3406/karst.1984.938

Guglielmetti, L., Poletto, F., Corubolo, P., Bitri, A., Dezayes, C., Farina, B. M., Martin, F., Meneghini, F., Moscariello, A., Nawratil de Bono, C., & Schleifer, A. (2020). Results of a walk-above vertical seismic profiling survey acquired at the Thônex-01 geothermal well (Switzerland) to delineate fractured carbonate formations for geothermal development. *Geophysical Prospecting*, *68*(4), 1139–1153. https://doi.org/10.1111/1365-2478.12912

Guillaume, A., & Guillaume, S. (1969). *Notice explicative, Carte géol. France (1/50 000), Feuille Morez-Bois d'Amont (605)* [Explanatory notes]. Bureau Des Recherches Géologiques et Minières. http://ficheinfoterre.brgm.fr/Notices/0605N.pdf

Guillaume, S. (1966). *Le crétacé du Jura français* [Doctoral thesis]. Bureau Des Recherches Géologiques et Minières.

Haas, M., Carraro, D., Ventra, D., Plötze, M., De Haller, A., & Moscariello, A. (2022). Integrated stratigraphic, sedimentological and petrographical evaluation for CERN's Future Circular Collider subsurface infrastructure (Geneva Basin, Switzerland-France). *Swiss Journal of Geosciences*, *115*(1), 16. https://doi.org/10.1186/s00015-022-00407-y

Herb, R. (1988). Eocaene Paläogegographie und Paläotektonik des Helvetikums. *Eclogae Geologicae Helvetiae*, *81*(3), 611–657. https://doi.org/10.5169/seals-166197

Hooker, J. J., & Weidmann, M. (2000). *The Eocene mammal faunas of Mormont, Switzerland. Systematic revision and resolution of dating problems* (Vol. 120). Schweitzerische Paläontologische Abhandlungen.

Hooker, J. J., & Weidmann, M. (2007). A diverse rodent fauna from the middle Bartonian (Eocene) of Les Alleveys, Switzerland: snapshot of the early theridomyid radiation. *Swiss Journal of Geosciences*, *100*(3), 469–493. https://doi.org/10.1007/s00015-007-1241-1

Hörbrand, T., Beichel, K., Bendias, D., Savvatis, A., & Kohl, T. (2024). Karst control on reservoir performance of a developed carbonate geothermal reservoir in Munich, Germany. *Geological Society, London, Special Publications*, *548*(1), 291–310. https://doi.org/10.1144/sp548-2024-42

Hutcheon, I. (1990). *Clay-carbonate reactions in the Venture area, Scotian Shelf, Nova Scotia, Canada* (Vol. 2, pp. 199–212).

Iljima, A., & Matsumoto, R. (1982). Berthierine and Chamosite in Coal Measures of Japan. *Clays and Clay Minerals*, *30*(4), 264–274. https://doi.org/10.1346/ccmn.1982.0300403

Jeannottat, S. (2005). *Etude paléopédologique de vertisols dans un système fluviatile (Marnière d'Epéclens, USM du plateau): et Cartographie des formations superficielles du Cirque de St-Sulpice, Jura neuchâtelois, Suisse* [Doctoral thesis, Université de Neuchâtel]. https://libra.unine.ch/handle/20.500.14713/28751

Jenny, Ja., Burri, J.-P., Muralt, R., Pugin, A., Schegg, R., Ungemach, P., Vuataz, F.-D., & Wernli, R. (1995). Le forage géothermique de Thônex (Canton de Genève): Aspects stratigraphiques, tectoniques, diagénétiques, géophysiques et hydrogéologiques. *Eclogae Geologicae Helvetiae*, *88*(2), 365–396.

Jordi, H. A. (1995). *Notice explicative, Atlas géologique de la Suisse (1/25 000), 1203 Yverdon-les-Bains, Feuille 94* [Explanatory notes]. Service Hydrologique et Géologique National.

Joukowsky, E., & Favre, J. (1913). *Monographie géologique et paléontologique du Salève: Haute-Savoie: Vol. 37(4): Mémoires de La Société de Physique et d'Histoire Naturelle de Genève*.

Kázmér, M., Dunkl, I., Frisch, W., Kuhlemann, J., & OzsvÁrt, P. (2003). The Palaeogene forearc basin of the Eastern Alps and Western Carpathians: subduction erosion and basin evolution. *Journal of the Geological Society*, *160*(3), 413–428. https://doi.org/10.1144/0016-764902-041

Kelemen, P., Dunkl, I., Csillag, G., Mindszenty, A., Józsa, S., Fodor, L., & von Eynatten, H. (2022). Origin, timing and paleogeographic implications of Paleogene karst bauxites in the northern Transdanubian range, Hungary. *International Journal of Earth Sciences*, *112*(1), 243–264. https://doi.org/10.1007/s00531-022-02249-3

Kerrien, Y., Turrel, C., Monjuvent, G., Charollais, J., Lombard, A., Balmer, F., Olmari, F., Papillon, R., Fontannaz, L., Amberger, G., Ruchat, C., Grebert, Y., & Marthaler, M. (1998). *Carte géol. France (1/50 000), feuille Annemasse (654)* [Geologic map]. Bureau Des Recherches Géologiques et Minières.

Kocurek, G., Lancaster, N., Carr, M., & Frank, A. (1999). Tertiary Tsondab Sandstone Formation: preliminary bedform reconstruction and comparison to modern Namib Sand Sea dunes. *Journal of African Earth Sciences*, *29*(4), 629–642. https://doi.org/10.1016/S0899-5362(99)00120-7

Kok, J. F., Parteli, E. J. R., Michaels, T. I., & Karam, D. B. (2012). The physics of wind-blown sand and dust. *Reports on Progress in Physics*, *75*(10), 106901. https://doi.org/10.1088/0034-4885/75/10/106901

Lancaster, N. (2020). Dune morphology, chronology, and Quaternary climatic change. In *Quaternary Deserts and Climatic Change* (1st ed., pp. 339–349). https://doi.org/10.1201/9781003077862-35

Liu, B., & Coulthard, T. J. (2015). Mapping the interactions between rivers and sand dunes: Implications for fluvial and aeolian geomorphology. *Geomorphology*, *231*, 246–257. https://doi.org/10.1016/j.geomorph.2014.12.011

Lombard, A. (1965). *Feuille 1301 Genève. Atlas géologique de la Suisse 1/25000* [Geologic map]. Commision Géologique Suisse.

Mack, G. H., James, W. C., & Monger, H. C. (1993). Classification of paleosols. *Geological Society of America Bulletin*, *105*(2), 129–136. https://doi.org/10.1130/0016-7606(1993)105<0129:cop>2.3.co;2

Maghfouri, S., Rastad, E., Mousivand, F., Choulet, F., & Ye, L. (2017). Geological and geochemical constraints on the Cheshmeh-Frezi volcanogenic stratiform manganese deposit, southwest Sabzevar basin, Iran. *Ore Geology Reviews*, *89*, 96–113. https://doi.org/10.1016/j.oregeorev.2017.06.015

Martini, J. (1962). Note sur le Tertiaire des environs de Mornex (Hte-Savoie). *Archives Des Sciences*, *15*(3), 619–626. https://doi.org/10.5169/seals-738684

Martini, J. (1965). Étude des minéraux secondaires du sidérolithique des environs de Genève. *Archives De Sciences*, *18*(1), 71–81. https://doi.org/10.5169/seals-739170

Mathey, B. (1976). *Hydrogéologie des bassins de la Serrière et du Seyon, Neuchâtel, Suisse* [Doctoral thesis, Université de Neuchâtel]. libra. https://doi.org/10.35662/unine-thesis-870

Matonti, C., Lamarche, J., Guglielmi, Y., & Marié, L. (2012). Structural and petrophysical characterization of mixed conduit/seal fault zones in carbonates: Example from the Castellas fault (SE France). *Journal of Structural Geology*, *39*, 103–121. https://doi.org/10.1016/j.jsg.2012.03.003

Mazenot, G., Mein, P., & Vincent, J. (1955). Dépôts miocènes et dépôts quaternaires dans le sidérolithique du Mont Ceindre près de Lyon (Rhône). *Bulletin mensuel de la Société linnéenne de Lyon*, *24*(4), 83–86. https://doi.org/10.3406/linly.1955.7718

Menkveld-Gfeller, U., Kempf, O., & Funk, H. (2016). Lithostratigraphic units of the Helvetic Palaeogene: review, new definition, new classification. *Swiss Journal of Geosciences*, *109*(2), 171–199. https://doi.org/10.1007/s00015-016-0217-4

Methner, K., Mulch, A., Fiebig, J., Wacker, U., Gerdes, A., Graham, S. A., & Chamberlain, C. P. (2016). Rapid Middle Eocene temperature change in western North America. *Earth and Planetary Science Letters*, *450*, 132–139. https://doi.org/10.1016/j.epsl.2016.05.053

Meunier, A. (2005). *Clays* (1st ed.). Springer. https://doi.org/10.1007/b138672

Michard, A. (2002). The Eocene unconformity of the Briançonnais domain in the French–Italian Alps, revisited (Marguareis massif, Cuneo); a hint for a Late Cretaceous–Middle Eocene frontal bulge setting. *Geodinamica Acta*, *15*(5–6), 289–301. https://doi.org/10.1016/s0985-3111(02)01094-x

Micheletti, F., Fornelli, A., Spalluto, L., Parise, M., Gallicchio, S., Tursi, F., & Festa, V. (2023). Petrographic and Geochemical Inferences for Genesis of Terra Rossa: A Case Study from the Apulian Karst (Southern Italy). *Minerals*, *13*(4), 499. https://doi.org/10.3390/min13040499

Mindszenty, A., Szintai, M., Tóth, K., Szantner, F., Nagy, T., Gellai, M., & Baross, G. (1988). Sedimentology and depositional environment of the Csabpuszta bauxite (Paleocene/Eocene) in the South Bakony Mts., Hungary. *Acta Geologica Hungarica*, *31*(3–4), 339–370.

Mongelli, G., Boni, M., Buccione, R., & Sinisi, R. (2014). Geochemistry of the Apulian karst bauxites (southern Italy): Chemical fractionation and parental affinities. *Ore Geology Reviews*, *63*, 9–21. https://doi.org/10.1016/j.oregeorev.2014.04.012

Moore, C. H., & Wade, W. J. (Eds.). (2013). *Carbonate Reservoirs - Porosity and Diagenesis in a Sequence Stratigraphic Framework: Vol. 67: Developments in Sedimentology* (2nd ed.). Elsevier.

Morad, S., Al-Ramadan, K., Ketzer, J. M., & De Ros, L. F. (2010). The impact of diagenesis on the heterogeneity of sandstone reservoirs: A review of the role of depositional facies and sequence stratigraphy. *AAPG Bulletin*, *94*(8), 1267–1309. https://doi.org/10.1306/04211009178

Morsilli, M., Hairabian, A., Borgomano, J., Nardon, S., Adams, E., & Gartner, G. B. (2017). The Apulia Carbonate Platform—Gargano Promontory, Italy (Upper Jurassic–Eocene). *AAPG Bulletin*, *101*(04), 523–531. https://doi.org/10.1306/011817dig17031

Moscariello, A. (2019). Exploring for geo-energy resources in the Geneva Basin (Western Switzerland): opportunities and challenges. *Swiss Bulletin Für Angewandte Geologie*, *24*(2), 105–124. https://archive-ouverte.unige.ch/unige:131617

Moscariello, A. (2021). The Geomorphological Landscapes in the Geneva Basin. In *Landscapes and Landforms of Switzerland* (pp. 83–96). https://doi.org/10.1007/978-3-030-43203-4_6

Moscariello, A., Gorin, G., Charollais, J., & Russillon, E. (2014). *Geology of Western Switzerland and nearby France in a Geo-Energy perspective*. 19th International Sedimentological Congress, Geneva, Switzerland.

Moscariello, A., Guglielmetti, L., Omodeo Sale, S., De Haller, A., Eruteya, O., Lo, H. Y., Clerc, N., Makhloufi, Y., Do Couto, D., Ferreira De Oliveira, G., Perozzi, L., DeOliveira, F., Hollmuller, P., Quiquerez, L., Nawratil De Bono, C., Martin, F., & Meyer, M. (2020). Heat production and storage in Western Switzerland: advances and challenges of intense multidisciplinary geothermal exploration activities, an 8 years progress report. *Proceedings*. World Geothermal Congress, Reykjavik, Iceland. https://archive-ouverte.unige.ch/unige:127903

Mountney, N. P. (2011). A stratigraphic model to account for complexity in aeolian dune and interdune successions. *Sedimentology*, *59*(3), 964–989. https://doi.org/10.1111/J.1365-3091.2011.01287.X

Mulch, A., Chamberlain, C. P., Cosca, M. A., Teyssier, C., Methner, K., Hren, M. T., & Graham, S. A. (2015). Rapid change in high-elevation precipitation patterns of western North America during the Middle Eocene Climatic Optimum (MECO). *American Journal of Science*, *315*(4), 317–336. https://doi.org/10.2475/04.2015.02

Narayan, N. S., Adams, C. A., & Gluyas, J. G. (2021). Karstified and fractured Lower Carboniferous (Mississippian) limestones of the UK − A cryptic geothermal reservoir. *Zeitschrift Der Deutschen Gesellschaft Für Geowissenschaften*, *172*(3), 251–265. https://doi.org/10.1127/zdgg/2021/0288

Nesbitt, H. W., & Young, G. M. (1982). Early Proterozoic climates and plate motions inferred from major element chemistry of lutites. *Nature*, *299*(5885), 715–717. https://doi.org/10.1038/299715a0

Olivetti, V., Balestrieri, M. L., Godard, V., Bellier, O., Gautheron, C., Valla, P. G., Zattin, M., Faccenna, C., Pinna-Jamme, R., & Manchuel, K. (2020). Cretaceous and late Cenozoic uplift of a Variscan Massif: The case of the French Massif Central studied through low-temperature thermochronometry. *Lithosphere*, *12*(1), 133–149. https://doi.org/10.1130/l1142.1

Öztürk, H., Hein, J. R., & Hanilçi, N. (2002). Genesis of the Dogankuzu and Mortas Bauxite Deposits, Taurides, Turkey: Separation of Al, Fe, and Mn and Implications for Passive Margin Metallogeny. *Economic Geology*, *97*(5), 1063–1077. https://doi.org/10.2113/gsecongeo.97.5.1063

Pepe, M., & Parise, M. (2014). Structural control on development of karst landscape in the Salento Peninsula (Apulia, SE Italy). *Acta Carsologica*, *43*(1), 101–114. https://doi.org/10.3986/ac.v43i1.643

Peris Cabré, S., Valero, L., Spangenberg, J. E., Vinyoles, A., Verité, J., Adatte, T., Tremblin, M., Watkins, S., Sharma, N., Garcés, M., Puigdefàbregas, C., & Castelltort, S. (2023). Fluvio-deltaic record of increased sediment transport during the Middle Eocene Climatic Optimum (MECO), Southern Pyrenees, Spain. *Climate of the Past*, *19*(3), 533–554. https://doi.org/10.5194/cp-19-533-2023

Pettijohn, F. J., Potter, P. E., & Siever, R. (1972). Petrographic Classification and Glossary. In *Sand and sandstone* (1st ed., pp. 149–174). Springer. https://doi.org/10.1007/978-1-4615-9974-6_5

Pfiffner, O. A. (2014). *Geology of the Alps* (2nd ed.). Wiley-Blackwell.

Pharaoh, T., Jones, D., Kearsey, T., Newell, A., Abesser, C., Randles, T., Patton, A., & Kendall, R. (2021). Early Carboniferous limestones of southern and central Britain: Characterisation and preliminary assessment of deep geothermal prospectivity. *Zeitschrift Der Deutschen Gesellschaft Für Geowissenschaften*, *172*(3), 227–249. https://doi.org/10.1127/zdgg/2021/0282

Pictet, A. (2021). New insights on the Early Cretaceous (Hauterivian–Barremian) Urgonian lithostratigraphic units in the Jura Mountains (France and Switzerland): the Gorges de l'Orbe and the Rocher des Hirondelles formations. *Swiss Journal of Geosciences*, *114*(1), 1–47. https://doi.org/10.1186/s00015-021-00395-5

Pictet, A., Delamette, M., & Matrion, B. (2016). The Perte-du-Rhône Formation, a new Cretaceous (Aptian-Cenomanian) lithostratigraphic unit in the Jura mountains (France and Switzerland). *Swiss Journal of Geosciences*, *109*(2), 221–240. https://doi.org/10.1007/s00015-016-0220-9

Pittman, E. D., Larese, R. E., & Heald, M. T. (1992). Clay Coats: Occurrence and Relevance to Preservation of Porosity in Sandstones. In D. W. Houseknecht & E. D. Pittman (Eds.), *Origin, Diagenesis and Petrophysics of Clay Minerals in Sandstones: Vol. 47: SEPM Special Publication* (pp. 241–255). https://doi.org/10.2110/pec.92.47.0241

Postma, D. (1982). Pyrite and siderite formation in brackish and freshwater swamp sediments. *American Journal of Science*, *282*(8), 1151–1183. https://doi.org/10.2475/ajs.282.8.1151

Pye, K., & Tsoar, H. (2009). *Aeolian Sand and Sand Dunes*. Springer. https://doi.org/10.1007/978-3-540-85910-9

Radwan, A. E. (2020). Modeling the Depositional Environment of the Sandstone Reservoir in the Middle Miocene Sidri Member, Badri Field, Gulf of Suez Basin, Egypt: Integration of Gamma-Ray Log Patterns and Petrographic Characteristics of Lithology. *Natural Resources Research*, *30*(1), 431–449. https://doi.org/10.1007/s11053-020-09757-6

Renevier, E. (1877). Eocène supérieur des Alpes vaudoises et sidérolithique du Jura. *Bulletin de La Société Géologique de France*, *2ième série*(V), 1–793.

Retallack, G. J. (1997). Early Forest Soils and Their Role in Devonian Global Change. *Science*, *276*(5312), 583–585. https://doi.org/10.1126/science.276.5312.583

Sánchez-Román, M., Vasconcelos, C., Schmid, T., Dittrich, M., McKenzie, J. A., Zenobi, R., & Rivadeneyra, M. A. (2008). Aerobic microbial dolomite at the nanometer scale: Implications for the geologic record. *Geology*, *36*(11), 879. https://doi.org/10.1130/g25013A.1

Schegg, R., & Leu, W. (1996). Clay Mineral Diagenesis and Thermal History of the Thonex Well, Western Swiss Molasse Basin. *Clays and Clay Minerals*, *44*(5), 693–705. https://doi.org/10.1346/ccmn.1996.0440513

Schellmann, W. (1986). A new definition of laterite. *Memoirs of the Geological Survey of India*, *120*, 1–7.

Schoeller, H. (1941). Étude sur le sidérolithique du Lot et du Lot-et-Garonne. *Bulletin Du Service de La Carte Géologique de La France*, *43*(206), 1–19.

Schölderle, F., Lipus, M., Pfrang, D., Reinsch, T., Haberer, S., Einsiedl, F., & Zosseder, K. (2021). Monitoring cold water injections for reservoir characterization using a permanent fiber optic installation in a geothermal production well in the Southern German Molasse Basin. *Geothermal Energy*, *9*(1), 1–36. https://doi.org/10.1186/S40517-021-00204-0/FIGURES/15

Schölderle, F., Pfrang, D., Ernst, V., Winter, T., & Zosseder, K. (2025). Productivity zoning and petrophysical assessment in the Munich metropolitan area for hydro-geothermal utilization using multivariate methods. *Geothermal Energy*, *13*(1), 1–41. https://doi.org/10.1186/S40517-025-00342-9/FIGURES/22

Schölderle, F., Pfrang, D., & Zosseder, K. (2023). Inverse flow zone characterization using distributed temperature sensing in a deep geothermal production well located in the Southern German Molasse Basin. *Advances in Geosciences*, *58*, 101–108. https://doi.org/10.5194/adgeo-58-101-2023

Schumacher, M. E. (2002). Upper Rhine Graben: Role of preexisting structures during rift evolution. *Tectonics*, *21*(1), 6–17. https://doi.org/10.1029/2001tc900022

Schweitzer, J. S., Ellis, D. V., Grau, J. A., & Hertzog, R. C. (1988). Elemental concentrations from gamma ray spectroscopy logs. *The International Journal of Radiation Applications and Instrumentation, Part E (Nuclear Geophysics)*, *2*(3), 175–181.

Séranne, M., Camus, H., Lucazeau, F., Barbarand, J., & Quinif, Y. (2002). Surrection et érosion polyphasées de la bordure cévenole. Un exemple de morphogenèse lente. *Bulletin de La Société Géologique de France*, *173*(2), 97–112. https://doi.org/10.2113/173.2.97

Sesiano, J. (2017). Des fours catalans au sommet du Salève: la sidérurgie aux portes de Genève. *Nature Et Patrimoine En Pays De Savoie*, *52*, 19–22.

Sharma, N., Spangenberg, J. E., Adatte, T., Vennemann, T., Kocsis, L., Vérité, J., Valero, L., & Castelltort, S. (2024). Middle Eocene Climatic Optimum (MECO) and its imprint in the continental Escanilla Formation, Spain. *Climate of the Past*, *20*(4), 935–949. https://doi.org/10.5194/cp-20-935-2024

Sial, A. N., Lacerda, L. D., Ferreira, V. P., Frei, R., Marquillas, R. A., Barbosa, J. A., Gaucher, C., Windmöller, C. C., & Pereira, N. S. (2013). Mercury as a proxy for volcanic activity during extreme environmental turnover: The Cretaceous–Paleogene transition. *Palaeogeography, Palaeoclimatology, Palaeoecology*, *387*, 153–164. https://doi.org/10.1016/j.palaeo.2013.07.019

SIG. (2020). *Subvention OFEN et résultats du forage de Lully (Dossier de presse)*.

Simon-Coinçon, R., Thiry, M., & Quesnel, F. (2000). Paléopaysages et paléoenvironnements sidérolithiques du Nord du Massif central (France). *Comptes Rendus de l'Académie des Sciences - Series IIA - Earth and Planetary Science*, *330*(10), 693–700. https://doi.org/10.1016/s1251-8050(00)00189-0

Singer, A. (1984). Pedogenic Palygorskite in the Arid Environment. In A. Singer & E. Galan (Eds.), *Palygorskite — Sepiolite: Occurrences, Genesis and Uses: Vol. 37: Developments in Sedimentology* (pp. 169–176). Elsevier. https://doi.org/10.1016/s0070-4571(08)70036-0

Sissingh, W. (1997). Tectonostratigraphy of the North Alpine Foreland Basin: correlation of Tertiary depositional cycles and orogenic phases. *Tectonophysics*, *282*(1–4), 223–256. https://doi.org/10.1016/s0040-1951(97)00221-7

Smeraglia, L., Looser, N., Fabbri, O., Choulet, F., Guillong, M., & Bernasconi, S. M. (2021). U–Pb dating of middle Eocene–Pliocene multiple tectonic pulses in the Alpine foreland. *Solid Earth*, *12*(11), 2539–2551. https://doi.org/10.5194/se-12-2539-2021

Stampfli, G. M., Mosar, J., Marquer, D., Marchant, R., Baudin, T., & Borel, G. (1998). Subduction and obduction processes in the Swiss Alps. *Tectonophysics*, *296*(1–2), 159–204. https://doi.org/10.1016/s0040-1951(98)00142-5

Strasser, A., Charollais, J., Conrad, M. A., Clavel, B., Pictet, A., & Mastrangelo, B. (2016). The Cretaceous of the Swiss Jura Mountains: an improved lithostratigraphic scheme. *Swiss Journal of Geosciences*, *109*(2), 201–220. https://doi.org/10.1007/s00015-016-0215-6

Thiry, M., & Turland, M. (1985). Paléotoposéquences de sols ferrugineux et de cuirassements siliceux dans le sidérolithique du Nord du Massif Central (bassin de Montluçon-Domérat). *Géologie De France*, *2*, 175–192.

Thurmann, J. (1832). *Essai sur les soulèvements jurassiques du Porrentruy*. Librairie Parisienne.

Tremblin, M., Khozyem, H., Adatte, T., Spangenberg, J. E., Fillon, C., Grauls, A., Hunger, T., Nowak, A., Läuchli, C., Lasseur, E., Roig, J.-Y., Serrano, O., Calassou, S., Guillocheau, F., & Castelltort, S. (2022). Mercury enrichments of the Pyrenean foreland basins sediments support enhanced volcanism during the Paleocene-Eocene thermal maximum (PETM). *Global and Planetary Change*, *212*, 103794. https://doi.org/10.1016/j.gloplacha.2022.103794

Triat, J.-M. (1982). Paléoaltérations dans le crétacé supérieur de Provence rhodanienne. *Sciences Géologiques, Bulletins et Mémoires*, *68*.

Triat, J.-M., & Guendon, J. L. (1975). Les ocres d'Apt dans la région de Rustrel (Vaucluse): Paléoaltérations continentales de sédiments marins crétacés. *Travaux Des Laboratoires Des Sciences de La Terre. Série A*, *7*, 72.

Troesch, A. (1908). Beiträge zur Geologie der westlichen Kientaleralpen (Blümlisalpgrüppe). *Eclogae Geologicae Helvetiae*, *10*(1), 63–149. https://doi.org/10.5169/seals-156857

Tućan, F. (1912). *Terra rossa, deren Natur und Entstehung*. E. Schweizerbart.

Tucker, M. E., & Wright, V. Paul. (2009). *Carbonate sedimentology*. Wiley-Blackwell. https://doi.org/10.1002/9781444314175 van der Boon, A., Kuiper, K. F., van der Ploeg, R., Cramwinckel, M. J., Honarmand, M., Sluijs, A., & Krijgsman, W. (2021). Exploring a link between the Middle Eocene Climatic Optimum and Neotethys continental arc flare-up. *Climate of the Past*, *17*(1), 229–239. https://doi.org/10.5194/cp-17-229-2021

Van Lith, Y., Warthmann, R., Vasconcelos, C., & Mckenzie, J. A. (2003). Sulphate-reducing bacteria induce low-temperature Ca-dolomite and high Mg-calcite formation. *Geobiology*, *1*(1), 71–79. https://doi.org/10.1046/j.1472-4669.2003.00003.x

Van Wagoner, J. C., Mitchum, R. M., Campion, K. M., & Rahmanian, V. D. (1990). *Siliciclastic Sequence Stratigraphy in Well Logs, Cores, and Outcrops: Concepts for High-Resolution Correlation of Time and Facies: Vol. 7:AAPG Methods in Explortation Series*. https://doi.org/10.1306/Mth7510

Varadachari, C., Goswami, G., & Ghosh, K. (2006). Dissolution of iron oxides. *Clay Research*, *25*(1), 1–22.

Vernet, J.-P. (1958). Etudes sédimentologiques et pétrographiques des formations tertiaires et quaternaires de la partie occidentale du Plateau suisse. *Eclogae Geologicae Helvetiae*, *51*(3), 1115–1152.

Vernet, J.-P. (1963). Le Sidérolithique du Mormont (Vaud). *Bulletin de La Société Vaudoise Des Sciences Naturelles*, *68*(312), 313–332. https://doi.org/10.5169/seals-275449

Vial, R., Conrad, M. A., & Charollais, J. (1989). *Notice explicative, Carte géol. France (1/50 000), feuille Douvaine (629)* [Explanatory notes]. Bureau Des Recherches Géologiques et Minières. http://ficheinfoterre.brgm.fr/Notices/0629N.pdf

von Tavel, H. (1936). Stratigraphie der Balmhorngruppe mit Einschluss des Gemmipasses (Berner Oberland). *Mitteilungen Der Naturforschenden Gesellschaft Bern*, 43–120. https://doi.org/10.5169/seals-319381

Vuillemin, A., Wirth, R., Kemnitz, H., Schleicher, A. M., Friese, A., Bauer, K. W., Simister, R., Nomosatryo, S., Ordoñez, L., Ariztegui, D., Henny, C., Crowe, S. A., Benning, L. G., Kallmeyer, J., Russell, J. M., Bijaksana, S., Vogel, H., & The Towuti Drilling Project Science Team. (2019). Formation of diagenetic siderite in modern ferruginous sediments. *Geology*, *47*(6), 540–544. https://doi.org/10.1130/g46100.1

Waltham, A. C., & Fookes, P. G. (2003). Engineering classification of karst ground conditions. *Quarterly Journal of Engineering Geology and Hydrogeology*, *36*(2), 101–118. https://doi.org/10.1144/1470-9236/2002-33

Wang, B., Gong, J., Zuza, A. V., Liu, R., Bian, S., Tian, Y., Yang, X., Zhang, D., & Chen, H. (2021). Aeolian sand dunes alongside the Yarlung River in southern Tibet: A provenance perspective. *Geological Journal*, *56*(5), 2625–2636. https://doi.org/10.1002/gj.4058

Warren, J. (2000). Dolomite: occurrence, evolution and economically important associations. *Earth-Science Reviews*, *52*(1–3), 1–81. https://doi.org/10.1016/s0012-8252(00)00022-2

Warthmann, R., van Lith, Y., Vasconcelos, C., McKenzie, J. A., & Karpoff, A. M. (2000). Bacterially induced dolomite precipitation in anoxic culture experiments. *Geology*, *28*(12), 1091–1094. https://doi.org/10.1130/0091-7613(2000)28<1091:bidpia>2.0.co;2

Weidmann, M. (1984). Paléokarst éocène dans l'autochtone chablaisien (VS et VD). *Bulletin de La Murithienne*, *102*, 119–128.

Westerhold, T., Röhl, U., McCarren, H. K., & Zachos, J. C. (2009). Latest on the absolute age of the Paleocene–Eocene Thermal Maximum (PETM): New insights from exact stratigraphic position of key ash layers + 19 and - 17. *Earth and Planetary Science Letters*, *287*(3–4), 412–419. https://doi.org/10.1016/j.epsl.2009.08.027

Wieland, B. (1976). *Petrographie eozäner siderolithischer Gesteine des Helvetikums der Schweiz: ihre Diagenese und schwache Metamorphose* [Doctoral thesis]. Universität Bern.

Wieland, B. (1979). Zur Diagnese und schwachen Metamorphose eozaener siderolithischer Gesteine des Helvetikums. *Schweizerische Mineralogische Und Petrographische Mitteilungen*, *59*, 41–66. https://doi.org/10.5169/seals-46042

Wilkinson, C. M., Ganerød, M., Hendriks, B. W. H., & Eide, E. A. (2017). Compilation and appraisal of geochronological data from the North Atlantic Igneous Province (NAIP). In G. Péron-Pinvidic, J. R. Hopper, T. Funck, M. S. Stoker, C. Gaina, J. C. Doornenbal, & U. E. Árting (Eds.), *The NE Atlantic Region. A Reappraisal of Crustal Structure, Tectonostratigraphy and Magmatic Evolution: Vol. 447: Special Publications*. Geological Society of London. https://doi.org/10.1144/SP447.10

Wright, V. P. (2008). Calcrete. In D. J. Nash & S. J. McLaren (Eds.), *Geochemical Sediments and Landscapes* (pp. 10–45). Wiley-Blackwell. https://doi.org/10.1002/9780470712917.CH2

Wright, V. P., & Tucker, M. E. (2009). *Calcretes*. Wiley-Blackwell. https://doi.org/10.1002/9781444304497

Zachos, J. C., McCarren, H., Murphy, B., Röhl, U., & Westerhold, T. (2010). Tempo and scale of late Paleocene and early Eocene carbon isotope cycles: Implications for the origin of hyperthermals. *Earth and Planetary Science Letters*, *299*(1–2), 242–249. https://doi.org/10.1016/j.epsl.2010.09.004

Zachos, J. C., Pagani, M., Sloan, L., Thomas, E., & Billups, K. (2001). Trends, Rhythms, and Aberrations in Global Climate 65 Ma to Present. *Science*, *292*(5517), 686–693. https://doi.org/10.1126/science.1059412

Zachos, J. C., Wara, M. W., Bohaty, S., Delaney, M. L., Petrizzo, M. R., Brill, A., Bralower, T. J., & Premoli-Silva, I. (2003). A Transient Rise in Tropical Sea Surface Temperature during the Paleocene-Eocene Thermal Maximum. *Science*, *302*(5650), 1551–1554. https://doi.org/10.1126/science.1090110

Zhang, F., Xu, H., Konishi, H., Kemp, J. M., Roden, E. E., & Shen, Z. (2012). Dissolved sulfide-catalyzed precipitation of disordered dolomite: Implications for the formation mechanism of sedimentary dolomite. *Geochimica et Cosmochimica Acta*, *97*, 148–165. https://doi.org/10.1016/j.gca.2012.09.008

Ziegler, P. A. (1992). European Cenozoic rift system. *Tectonophysics*, *208*(1–3), 91–111. https://doi.org/10.1016/0040-1951(92)90338-7

Zosseder, K., Pfrang, D., Schölderle, F., Bohnsack, D., & Konrad, F. (2022). Characterisation of the Upper Jurassic geothermal reservoir in the South German Molasse Basin as basis for a potential assessment to foster the geothermal installation development – Results from the joint research project Geothermal Alliance Bavaria. *Geomechanik Und Tunnelbau*, *15*(1), 17–24. https://doi.org/10.1002/geot.202100087

Zular, A., Utida, G., Cruz, F. W., Sawakuchi, A. O., Wang, H., Bícego, M., Giannini, P. C. F., Rodrigues, S. I., Garcia, G. P. B., Vuille, M., Sifeddine, A., Zocatelli, R., Turcq, B., & Mendes, V. R. (2018). The effects of mid-Holocene fluvio-eolian interplay and coastal dynamics on the formation of dune-dammed lakes in NE Brazil. *Quaternary Science Reviews*, *196*, 137–153. https://doi.org/10.1016/j.quascirev.2018.07.022